


Dynamics and observational signatures of shell-like black hole mimickersUlf Danielsson,¹ Luis Lehner,² and Frans Pretorius³¹*Uppsala University, Uppsala 751 20, Sweden*²*Perimeter Institute for Theoretical Physics, 31 Caroline Street, Waterloo, Ontario N2L 2Y5, Canada*³*Princeton University, Princeton 08544, New Jersey, USA* (Received 24 September 2021; accepted 13 October 2021; published 2 December 2021)

We undertake the task of studying the nonlinear dynamics of quantum gravity motivated alternatives to black holes that in the classical limit appear as ultracompact shells of matter. We develop a formalism that should be amenable to numerical solution in generic situations. For a concrete model, we focus on the spherically symmetric anti-de Sitter (AdS) black bubble—a shell of matter at the Buchdahl radius separating a Schwarzschild exterior from an AdS interior. We construct a numerical code to study the radial dynamics of and accretion onto AdS black bubbles, with exterior matter provided by scalar fields. In doing so, we develop numerical methods that could be extended to future studies beyond spherical symmetry. Regarding AdS black bubbles in particular, we find that the original prescription for the internal matter fluxes needed to stabilize the black bubble is inadequate in dynamical settings, and we propose a two-parameter generalization of the flux model to fix this. To allow for more efficient surveys of parameter space, we develop a simpler numerical model adapted to spherically symmetric bubble dynamics. We identify regions of parameter space that do allow for stable black bubbles and moreover allow control to a desired end state after an accretion episode. Based on these results, and evolution of scalar fields on black bubble backgrounds, we *speculate* on some observational consequences if what are currently presumed to be black holes in the Universe were actually black bubbles.

DOI: [10.1103/PhysRevD.104.124011](https://doi.org/10.1103/PhysRevD.104.124011)**I. INTRODUCTION**

Since the recognition of black hole entropy and formulation of the black hole information paradox, many efforts have focused on interpreting and reconciling such puzzling aspects of black holes. These, and related attempts to tame the singularities inside black holes, motivated consideration of “extensions” to black holes, altering their structure in the vicinity of the classical horizon and its interior. This has resulted in proposals for objects like fuzzballs [1], gravastars [2], black bubbles [3], etc.—see Ref. [4] for a review, which also describes many other exotic compact object (ECO) alternatives to black holes not necessarily motivated by quantum gravity considerations.

Recently, the ability to detect gravitational waves from merging stellar-mass compact object binaries (e.g., Refs. [5,6]) as well as to observe horizon scale physics of supermassive black holes (see Ref. [7]) has tremendously energized this field, motivating the search for observational consequences of ECO alternatives to Kerr black holes. However, the majority of existing models of ECOs has not been studied in dynamical, nonlinear settings, and for some, it is even uncertain how that might be done in theory. This is clearly an unfortunate state of affairs, even beyond the obvious need for predicting waveforms in mergers, as understanding the dynamical stability of isolated objects, or lack thereof, could eliminate some models and guide refinements to more viable ones.

Here, we focus on a subclass of ECO modeled as an ultracompact thin shell: a 2-sphere surface layer of matter close to the would-be horizon of the analogous black hole, but still at a macroscopic distance outside, that separates a nonsingular interior spacetime from the exterior, asymptotically flat spacetime. To realize the ultimate goal of studying the merger of two such objects, one must resort to numerical simulations. This requires the introduction of novel ideas and methods to deal with the new ingredients such an ECO would bring to a traditional numerical general relativity code: singular surface layers, matter fields (including a cosmological constant) confined to the surface and or exterior/interior spacetimes, new interactions between traditional matter fields and the surface, etc.

Before such novel techniques can be investigated, it is essential to begin with a viable ECO model. This requires both a classically well-posed problem of the spacetime and matter system at hand¹ and that the ECO solutions are dynamically stable. A promising candidate in this regard, that we will adopt,² is the anti-de Sitter (AdS) black bubbles proposed by Danielsson *et al.* [3]. This model has so far

¹Requiring mathematically sound equations together with suitable initial and boundary conditions.

²This is a convenient choice, though lessons derived in our studies are applicable to other models as well.

only been developed for nonrotating or slowly rotating spacetimes [8]. In the nonrotating case, a thin shell of matter in equilibrium at the Buchdahl radius separates an interior AdS spacetime from the exterior Schwarzschild spacetime. The matter, inspired by string theory constructions, consists of a relativistic gas attached to a membrane, with internal interactions between the components designed to react to external perturbations so as to keep the bubble stable. Another goal of this work then is to explore the stability of these bubbles beyond the quasistationary, linear regime investigated in Ref. [3].

As a first step toward an ultimate goal of exploring black bubble mergers, we will restrict attention to single, spherically symmetric black bubbles. In spherical symmetry, one can adapt the problem to the symmetry, avoiding many complications one would need to address in a generic scenario. However, we have intentionally tried to *not* do that as much as possible, often complicating the problem simply for the sake of introducing a feature that would be present in a nonsymmetric case. This includes not explicitly imposing the Israel junction conditions [9] (that in spherical symmetry by themselves can uniquely determine the shell dynamics and map between interior/exterior spacetimes), choosing a metric ansatz where we have gauge waves that propagate at the speed of light, and using a scalar field as a proxy for gravitational wave interactions with the shell.

In a sense, we have been successful in implementing this Einstein-Klein-Gordon-hydrodynamic (EKGH) model. However, when first applying it to AdS black bubbles, we found it failed to address the question of physical stability in the large-bubble limit, of interest for astrophysical applications. This turns out in part to be due to some of these “complicating” choices we made for the EKGH code and also in part due to the physics of black bubbles in the large mass limit. To answer the stability question, which would be crucial to do before either improving the EKGH code, or to go beyond spherical symmetry, we here also introduce a simpler, spherically symmetric adapted model that can investigate some aspects of the nonlinear, dynamical stability of large black bubbles.

The rest of the Introduction outlines the remainder of the paper and summarizes the main results.

In Sec. II, we review aspects of AdS black bubbles and give a general formalism to describe such $2 + 1$ -dimensional ($2 + 1$ D) matter embedded in a dynamical $3 + 1$ D spacetime. For surface matter, we consider the combination of fluids proposed in Ref. [3], though we allow for the possibility of viscosity to be present. For external matter, we consider two scalar fields: the first does not directly interact with the matter intrinsic to the shell, and can freely propagate across its surface (i.e., the proxy for gravitational waves), while the second can be absorbed by the shell to model accretion.

In Sec. III, we specialize to spherical symmetry. First, in Sec. III A, we describe the full EKHG version of the

equations, including our ansatz for the metric, the resultant evolution equations, constraint equations, initial conditions, and boundary conditions. In Sec. III E, we describe the simplified model that can explore the dynamics of an AdS black bubble perturbed by an unspecified external source (i.e., it does not include the gravitational wave proxy scalar field and cannot relate the perturbing source to a particular external scalar field profile).

Stability in the AdS black bubble model is achieved via an internal flux between the gas and brane components. In Sec. IV, we discuss this in more detail, including the extensions beyond that of the original model we introduce here. As outlined there, with more details and analysis given in Appendixes A and B, the flux prescription of Ref. [3] does not result in stable bubbles if the full dynamical problem is considered, and one demands the internal flux can only react to local changes in the environment. The modifications we have introduced here are somewhat *ad hoc*, though our reasoning is if we can identify flux prescriptions that lead to stable bubbles it will help guide searches for more fundamental physical mechanisms that can achieve similar effects.

In Sec. V, we discuss numerical implementation details of the spherically symmetric equations given in Sec. III. We focus on novel aspects pertaining to this problem, including a weak-form integration procedure to deal with the singular surface and a dual coordinate scheme to keep the bubble at a fixed location within the computational grid. More technical details of this are relegated to Appendixes C and D.

In Sec. VI, we give results from evolution of perturbed black bubbles. In Sec. VI A, we focus on the physics of AdS black bubble dynamics, giving examples using flux parameters (guided by the linear analysis presented in Appendix B) that allow for stable, large black bubbles. In Sec. VI B, we discuss the limitations of the EKGH code in this regard; in particular, the two (likely related) problems are the challenge to achieve sufficient accuracy over multiple light-crossing times and a “mass amplification” effect that occurs due to the purely gravitational interaction of scalar field energy crossing from the exterior to interior spacetimes. However, the EKGH code is capable of modeling the long term interactions of the scalar field on a *fixed* black bubble background; in this section, then, we also present some results for the case of the gravitational wave proxy field that can freely cross the bubble surface. This suggests some remarkable potential observational consequences following black bubble formation, in particular a slow, nearly monochromatic release of the energy at the fundamental oscillation frequency of the interior AdS spacetime, redshifted to near the characteristic frequency of the exterior black bubble spacetime. However, as estimated in Appendix E, if the AdS length scale is set by Planck scale physics, the energy release will be much too slow to be of relevance for astrophysical sized (stellar and

supermassive) black holes. Discriminating between black bubble and black hole mergers would then seem to require understanding the prompt signal following a collision, or unusual interior physics/anomalously large length scales; we speculate on these topics as well as give directions for future work in Sec. VII.

II. ADS BLACK BUBBLES AND GENERAL CONSIDERATIONS

Among suggested alternatives to black holes resulting from gravitational collapse are *black bubbles*, first proposed in Ref. [3]. Though their creation is argued to come from a quantum tunneling process and their surface structure is argued to be composed of string-theory inspired matter and higher-dimensional geometric constructions, once formed, astrophysically large black bubbles can to good approximation be described by classical physics. In this limit, they are solutions to four-dimensional Einstein gravity coupled to matter—an electromagnetic gas, a membrane, and a subleading stiff gas—confined to a thin shell. For the nonrotating case, the interior is AdS spacetime with a cosmological constant $\Lambda \equiv -\ell^2$, and the exterior is Schwarzschild with a gravitational mass m . For both stability and to possess an equation of state that “naturally” follows from the string theory construction, the shell is required to be at the Buchdahl radius $r = 9m/4$.

Of particular interest is to assess whether a black bubble can be regarded as a viable candidate for an “exotic” alternative to a black hole. Notably, this would mean confronting the behavior of merging black bubbles with gravitational wave observations of what are currently interpreted as merging black holes [10,11] and whether accretion onto supermassive black bubbles is distinguishable from that onto supermassive black holes as observed by the Event Horizon Telescope (EHT) [12].

Here, we focus on working toward the goal of using gravitational wave observations to study the viability of black bubbles. This requires that the classical system admits a well-posed initial value problem outside of the static, spherically symmetric spacetime ansatz where they were first analyzed and that single black bubbles are dynamically stable to generic perturbations. From the classical perspective, this would include nonlinear perturbations, at least as long as the energy of the perturbation is not large enough to require considering it a “creation event,” rather than a perturbation.³ In Ref. [3], a first step toward addressing the stability question was taken, and it was argued that several ingredients are necessary for black

bubbles to be stable under radial perturbations. The primary ones are that the gas comprising the bubble must be at the local Unruh (acceleration) temperature as measured by a comoving observer just outside the shell and that an internal flux between the relativistic gas and membrane components of the shell operates to react to perturbations to instantaneously maintain this temperature.

In this work, we take a couple of additional steps toward the goal of assessing the ultimate (classical) viability of black bubbles. The first is to study the stability of spherically symmetric bubbles undergoing dynamical radial perturbations, not necessarily small, excited by some external agent. As we show in Appendixes A and B, the original kinematic stability analysis of Ref. [3] missed a dynamical component of the 4-acceleration that feeds into the flux, the latter part of which has a destabilizing effect on the black bubble. Thus, the original flux prescription does not lead to stability, and in Sec. IV, we offer extensions to it that can lead to radially stable bubbles.

The second step is to formulate the problem in a manner that does not rely on spherical symmetry, even though our example implementation is restricted to it. The technical issue here is how to deal with singular (delta function) distributions of matter coupled to the Einstein equations in a situation without symmetries. In particular, in general, the shell world tube cannot be considered a spacetime boundary in a mathematical (or physical) sense where boundary conditions need to be applied; for example, gravitational waves can freely cross this location, and any influence the matter might exert on the gravitational waves is governed by the Einstein equations, not any “boundary condition” one places there. Of course, this is exactly where the Israel (sometimes also referred to as the Lanczos-Darmois-Israel-Sen) junction conditions come from, but in spherical symmetry, one *can* effectively employ them as boundary conditions for the spacetime on either side of the world tube (essentially because there are no gravitational waves in spherical symmetry). However, it is difficult to envision how such an approach could be extended to spacetimes without symmetries, in particular where the surface layer might not be the dominant source of curvature (for example, it would have to work in the limit of a “fictitious surface” where the stress energy of the surface goes to zero). Instead, as described next, we adopt a first principles approach, adding a distributional source for the shell matter to the Einstein equations, arriving at the junction conditions as a consequence rather than a condition put in *a priori*.

A. Formulation

For our target model, there are three distinct regions. An interior region, with a nonzero (negative) cosmological constant, an exterior region with $\Lambda = 0$, and a shell that separates them. The shell, with a nontrivial stress energy tensor composed of several matter components outlined below, provides the physical mechanism that

³That also begs the question of whether classical physics can even approximately address the coalescence phase of bubble mergers, especially in the comparable mass case where there would be a significant change in the mass of the final bubble compared to either progenitor. We leave that to future work to contemplate.

can, in principle, stabilize the shell. In addition, we add bulk scalar fields to model dynamical scenarios, both to perturb the black bubble via a gravitational interaction, and a direct interaction where the black bubble accretes scalar field energy. To account for all these ingredients, on a rather general footing, we proceed as follows. We consider the Einstein equations in the full spacetime (using units where Newton's constant $G = 1$ and the speed of light $c = 1$)

$$G_{ab} = 8\pi T_{ab}, \quad (1)$$

with a stress-energy tensor of the form

$$T_{ab} = {}^{(\rho)}T_{ab}\delta(s) + {}^{(\psi)}T_{ab} + {}^{(\xi)}T_{ab}\Theta(s) - \frac{\Lambda}{8\pi}g_{ab}\Theta(-s). \quad (2)$$

The net stress-energy tensor of the material comprising the shell is ${}^{(\rho)}T_{ab}$, ${}^{(\psi)}T_{ab}$ is that of a bulk scalar field that does not directly interact with shell material (but can cross the shell location from the outside to inside and vice versa), while ${}^{(\xi)}T_{ab}$ is that of an exterior-only scalar field that interacts with the shell via appropriately chosen boundary conditions, discussed below. The shell world tube is described by the level set scalar function $s(x^a) = 0$, with $\delta(s)$ the Dirac delta distribution, and $\Theta(s)$ is the Heaviside step function. Immediately adjacent to any point on the shell, we will normalize s to measure proper distance orthogonal to the shell at that point, with $s > 0$ ($s < 0$) on the outside (inside). The gradient $s_a \equiv s_{,a}$, dual to the vector $s^a = g^{ab}s_b$ normal to the world tube, will thus be unit ($s^a s_a = 1$) and defines the projection tensor $h_{ab} = g_{ab} - s_a s_b$ onto the shell, as well as the extrinsic curvature

$$K_{ab} = -h^c{}_a h^d{}_b \nabla_c s_d \quad (3)$$

evaluated on either side of the shell as used in the Israel junction conditions.

B. Scalar field and shell material

The stress-energy tensors for the scalar fields are

$${}^{(\psi)}T_{ab} = \nabla_a \psi \nabla_b \psi - \frac{1}{2} g_{ab} |\nabla \psi|^2, \quad (4)$$

$${}^{(\xi)}T_{ab} = \nabla_a \xi \nabla_b \xi - \frac{1}{2} g_{ab} |\nabla \xi|^2. \quad (5)$$

Following Ref. [3], we will build the shell from three fluid components: a relativistic gas, a brane, and a subleading stiff gas. There, all the fluids were modeled as perfect (ideal) fluids; here, we allow for viscosity to model dissipative effects. The latter is important to account for the entropy growth of the bubble as it interacts with its environment. Since the gas dominates the entropy of the

bubble, for simplicity, then, we only add dissipation to that component of the shell. To do so, we employ the formulation of viscous relativistic hydrodynamics, which only modifies the fluid description to first order in a gradient expansion [13–15]. Under certain conditions (including spherical symmetry), we can consider a single 4-velocity u^a to characterize the flow of all fluid elements, and for simplicity of notation, we will do that here. The resulting stress-energy tensor for the shell is

$${}^{(\rho)}T_{ab} \equiv {}^{(\rho_g)}T_{ab} + {}^{(\rho_s)}T_{ab} + {}^{(\rho_\tau)}T_{ab}, \quad (6)$$

$${}^{(\rho_g)}T_{ab} = (\rho_g + \mathcal{A})u_a u_b + (p_g + \Pi)\Delta_{ab}, \quad (7)$$

$${}^{(\rho_s)}T_{ab} = \rho_s u_a u_b + p_s \Delta_{ab}, \quad (8)$$

$${}^{(\rho_\tau)}T_{ab} = \rho_\tau u_a u_b + p_\tau \Delta_{ab}, \quad (9)$$

where $\Delta_{ab} = h_{ab} + u_a u_b$, ρ_g , ρ_s and ρ_τ are the (equilibrium) rest-frame energy densities of the gas, string and brane components, with corresponding pressures $p_g = \rho_g/2$, $p_s = \rho_s$, and $p_\tau = -\rho_\tau$, respectively. The viscous modifications to the gas stress energy are captured by \mathcal{A} and Π , defined as

$$\mathcal{A} = \tau_e [u^a D_a \rho_g + (\rho_g + p_g) D_a u^a], \quad (10)$$

$$\Pi = -\zeta D_a u^a + \tau_p [u^a D_a \rho_g + (\rho_g + p_g) D_a u^a], \quad (11)$$

where τ_e , τ_p , and ζ are transport coefficients that are functions of ρ_g and $D_a \equiv h^b{}_a \nabla_b$. In general, there are additional terms proportional to the shear tensor π^{ab} and heat flux \mathcal{Q}^a , but these vanish in spherical symmetry, so we drop them here for simplicity. ζ is the bulk viscosity coefficient; (τ_e , τ_p) are often ignored in relativistic hydrodynamics, though are required in the first order theory for causality and to allow for defining (locally at least) well-posed problems⁴ [13–15].

C. Matter equations of motion

For the scalar fields, we impose the usual massless wave equations

$$\square \psi = 0, \quad (12)$$

$$\square \xi = 0. \quad (13)$$

For the shell, the equations of motion stem from net stress-energy conservation. We will further demand that each

⁴Though this well-posed-ness result is obtained in a somewhat weaker sense than the traditional Sobolev criteria and with a nonunique entropy current, it has shown promising results in incipient applications [16].

component of the shell individually satisfies conservation of its respective stress-energy tensor, except for an external source term J^a to the gas component to allow for energy exchange with the scalar field ξ and an internal flux j^a between the gas and brane components (discussed more in Sec. IV):

$$D_b^{(\rho_g)} T^{ab} = J^a - j^a, \quad (14)$$

$$D_b^{(\rho_s)} T^{ab} = 0, \quad (15)$$

$$D_b^{(\rho_\tau)} T^{ab} = j^a. \quad (16)$$

Note that we do not explicitly add a source term to ξ 's equation of motion (13), as at the location of the shell we do not impose (13), but rather must specify boundary conditions for ξ there, and this will effectively compensate for J^a . In spherical symmetry, the only gradients that will be relevant for these boundary conditions are those in the u^a and s^a directions, and J^a , being intrinsic to the shell, can then only have a component in the u^a direction. So, to simplify the expressions below, we define

$$J_U \equiv u_c J^c, \quad (17)$$

$$\xi_S \equiv s^a \nabla_a \xi, \quad (18)$$

$$\xi_U \equiv u^a \nabla_a \xi. \quad (19)$$

For consistency with the Einstein equations, the net stress-energy tensor must satisfy

$$T^{ab}{}_{;b} = 0. \quad (20)$$

Evaluating this at the shell, substituting in the equations of motion wherever possible, and averaging $\nabla_a s_b$, $\nabla_a u_b$ related terms that are discontinuous across the shell,⁵ we can split the result into a piece tangent to the shell,

$$T^{ab}{}_{;b} u_a = \xi_U \xi_S + J_U = 0, \quad (21)$$

and one orthogonal to the shell,

$$T^{ab}{}_{;b} s_a = \frac{\xi_U^2 + \xi_S^2}{2} + [(\rho + P)\tilde{a} + P\tilde{K}] + \frac{\Lambda}{8\pi} = 0. \quad (22)$$

In the above, a tilde ($\tilde{}$) denotes the averaging; we have defined

$$\rho \equiv \rho_g + \mathcal{A} + \rho_\tau + \rho_s, \quad (23)$$

$$P \equiv p_g + \Pi + p_\tau + p_s; \quad (24)$$

⁵The averaging can be justified by integrating the equations in a small volume about the shell and taking the limit of the volume to zero; see Ref. [9].

K is the trace of the extrinsic curvature (3); and a is the radial acceleration of u^a :

$$a \equiv \nabla_a u^b u^a s_b. \quad (25)$$

The orthogonal piece (22) gives the equation of motion for the shell, while the tangential piece (21) constrains the interaction between the gas and scalar field:

$$J_U = -\xi_U \xi_S. \quad (26)$$

With this relation in hand, one immediately sees that a pure Dirichlet ($\xi_U = 0$) or Neumann ($\xi_S = 0$) boundary condition forces $J_U = 0$. These options effectively implement a reflection with no direct energy exchange to the gas [though kinetic energy will still be exchanged via (22)]. To have the black bubble mimic a black hole and always absorb energy, one can demand $J_U < 0$ [see (34) below]. An obvious choice for this, that we will use in the results presented later, is

$$\xi_U = \xi_S. \quad (27)$$

This is the analog of an ingoing radiation condition at the shell, assuming ξ takes the form $\xi \sim \xi(t + r)$ there. Note that in this case, the energy associated to the field ξ is absorbed by the gas.

III. RESTRICTING TO SPHERICAL SYMMETRY

So far, we have kept the presentation general, discussing in broad strokes the governing equations from a global spacetime point of view. To simplify the form of the equations, in a couple of instances, we already imposed restrictions consistent with spherical symmetry, though this did not change the basic structure of the equations (in particular using a single 4-velocity u^a to describe the shell trajectory and all local fluid velocities, and only considering energy exchange with the scalar field in this same direction). Here, we do specialize the equations to spherical symmetry.

First, in Sec. III A, we consider the full EKGH system of equations in spherical symmetry, giving a set of 1 + 1D partial differential equations (PDEs) to solve for the spacetime metric and scalar fields, and a set of ordinary differential equations (ODEs) for the position and fluid properties of the shell. However, as discussed in Sec. VI B, in the large mass limit of relevance for astrophysical black holes, the corresponding code for this system of equations is not adequate to study black bubble evolutions for the time needed to ascertain their stability. This is in part due to the large disparity of scales in the problem in that limit, as well as decisions we made toward the longer term goal of extending the code beyond spherical symmetry (i.e., if going beyond spherical symmetry was not of interest, choices better adapted to the problem could be made, in

particular with regard to the interior and exterior coordinate charts).

Though, just as crucial as having the correct tools to go beyond spherical symmetry is knowing that this is a sensible endeavor in the first place. Early cases examined with the EKGH code indicated that the original black bubble prescription is not dynamically stable, leading us to consider the additional ingredients added to the model described in this paper. However, a linear stability analysis including the new flux options and dissipation (Appendix B) shows that the stability properties can be very different for small bubbles (relative to the AdS length scale $1/\ell$) versus large bubbles. Thus, it would be suspect to use any conclusions of nonlinear stability obtained with the EKGH code in the small bubble case to decide whether it would be worth the considerable effort needed to first resolve its problems with large bubbles and then extend beyond spherical symmetry. Therefore, we implemented a simplified ODE model, described in Sec. III E, that allows us to explore nonlinear stability in the large mass limit, albeit without completely general scalar-field interactions as allowed by the EKGH system.

A. Einstein-Klein-Gordon-hydrodynamic system

The formalism described above does not require a coordinate chart that gives a continuous metric across the shell. Discontinuous charts are convenient in certain respects and would be simple to implement in a code in spherical symmetry. Though, again, we want to use methods that could be extended beyond spherical symmetry in a straightforward manner; to that end, we will use a metric ansatz which is continuous across the shell. Moreover, we will adopt the following ‘‘lightlike’’ ansatz for the metric so that the equations of motion bear close resemblance to the typical structure encountered in 3 + 1D scenarios:

$$ds^2 = e^{2B(r,t)}(-dt^2 + dr^2) + r^2 e^{2C(r,t)} d\Omega^2. \quad (28)$$

Beyond the obvious structure of the $r-t$ sector of the metric, what this lightlike ansatz does is allow one to write the Einstein evolution equations for B and C so that the principal parts of each are wave equations.

B. Evolution equations

Let $f(x^a) = r - R(t)$, so the shell is at $f = 0$, i.e., at $r = R(t)$. Then, $s_a = \nabla_a f / |\nabla f|$, the coordinate velocity of the shell is $V \equiv dR/dt$, $u^a = \gamma(1, V, 0, 0)$, and $s^a = \gamma(V, 1, 0, 0)$, with $\gamma = e^{-B}/\sqrt{1-V^2}$. To deal with the distributional matter of the shell in the numerical code, we will integrate the equations at the location of the shell in ‘‘weak form,’’ as described in more detail in Sec. VA 1. This involves integrating over a volume in the coordinate r . In the covariant form of the stress tensor (2), the shell is a

distribution in s , and to adapt to the integration in r , we use $\int \delta(s) dr = \int \delta(s)(dr/ds) ds = dr/ds|_{s=0}$. So, in anticipation of that, in the equations below, $\delta(s)$ has been replaced with $\delta(f) dr/ds$, where $dr/ds = e^{-B}\sqrt{1-V^2}$, and defining $\int \delta(f) dr = 1$. We will write the Einstein and scalar field equations in first order form, defining $z_t \equiv z_{,t}$ and $z_r \equiv z_{,r}$ for a variable $z(t, r)$. Then, evolution equations for B, C from the Einstein equations (1), the wave equations for ψ (31) and ξ (32), conservation equations (14)–(16) for the shell fluids, and the evolution equation for the shell location (22) are

$$\begin{aligned} \dot{C}_t - C'_r &= 4\pi\rho e^{2B}\delta(f)\frac{dr}{ds} - e^{2B}\ell^2\Theta(-f) \\ &\quad + 2(C_r^2 - C_t^2) + \frac{4C_r}{r} + \frac{1 - e^{2(B-C)}}{r^2}, \end{aligned} \quad (29)$$

$$\begin{aligned} \dot{B}_t - B'_r &= -4\pi(\rho + 2P)e^{2B}\delta(f)\frac{dr}{ds} \\ &\quad + 4\pi[\psi_r^2 - \psi_t^2 + (\xi_r^2 - \xi_t^2)\Theta(f)] \\ &\quad + C_t^2 - C_r^2 - \frac{2C_r}{r} - \frac{1 - e^{2(B-C)}}{r^2}, \end{aligned} \quad (30)$$

$$\dot{\psi}_t - \psi'_r = 2(\psi_t C_r - \psi_r C_t) + \frac{2\psi_r}{r}, \quad (31)$$

$$\dot{\xi}_t - \xi'_r = 2(\xi_t C_r - \xi_r C_t) + \frac{2\xi_r}{r}, \quad (32)$$

$$\begin{aligned} \dot{\rho}_g &= -(\dot{\rho}_g + F(\rho_g + p_g)) \cdot \left(F(1 + \tau_p/\tau_e) - \hat{B} + \frac{V\dot{V}}{1-V^2} + \frac{\dot{\tau}_e}{\tau_e} \right) \\ &\quad - F(\dot{\rho}_g + \dot{p}_g) - (\rho_g + p_g)\hat{F} + \frac{\zeta F^2}{\tau_e} \\ &\quad - \frac{e^B\sqrt{1-V^2}}{\tau_e} \cdot \left[\dot{\rho}_g + F(\rho_g + p_g) + J_U e^B \sqrt{1-V^2} - j \right] \end{aligned} \quad (33)$$

$$\begin{aligned} &= -\left(\dot{\rho}_g + \frac{3F\rho_g}{2} \right) \left(\frac{3F}{2} - \hat{B} + \frac{V\dot{V}}{1-V^2} + \frac{\dot{\tau}_e}{\tau_e} \right) \\ &\quad - \frac{3}{2}(F\dot{\rho}_g + \hat{F}\rho_g) + \frac{\zeta F^2}{\tau_e} \\ &\quad - \frac{e^B\sqrt{1-V^2}}{\tau_e} \cdot \left[\dot{\rho}_g + \frac{3F\rho_g}{2} + J_U e^B \sqrt{1-V^2} - j \right], \end{aligned} \quad (34)$$

$$\begin{aligned} \dot{\rho}_s &= -(\rho_s + p_s)F \\ &= -2\rho_s F, \end{aligned} \quad (35)$$

$$\begin{aligned}\dot{\rho}_\tau &= -(\rho_\tau + p_\tau)F - j \\ &= -j,\end{aligned}\quad (36)$$

$$\begin{aligned}\dot{V} &= (1 - V^2) \left[\frac{2P(V\tilde{C}_t + \tilde{C}_r + 1/r)}{\rho} - (V\tilde{B}_t + \tilde{B}_r) \right. \\ &\quad \left. + \frac{e^B \sqrt{1 - V^2} (\ell^2 - 4\pi[\xi_U^2 + \xi_S^2])}{8\pi\rho} \right].\end{aligned}\quad (37)$$

In the above, an overdot ($\dot{}$) denotes the derivative with respect to t , and prime ($'$) denotes the derivative with respect to r . These equations are supplemented with “trivial” evolution equations for first order gradient variables, i.e., $\dot{z}_r = z'_r$ and $\dot{z} = z_r$. For each of the fluid evolution equations, a second expression is given where the relevant equation of state has been substituted in, and in the second expression for the viscous fluid τ_p has been replaced with $\tau_e/2$. The variable j denotes the component of the internal flux j^a in the direction of u^a . The fluid evolution requires derivatives of the metric intrinsic to the shell (which in spherical symmetry will only be along the u^a direction); for simplicity, we denote such gradients with hatted dots, and they can be computed with the 4D metric using appropriate combinations of r, t gradients, e.g., $\hat{B} = B_t + VB_r$ (and the combination is continuous across the shell despite the individual terms having jumps). We also introduced

$$F \equiv \dot{\mathbf{A}}/\mathbf{A} = 2(\hat{C} + V/r), \quad (38)$$

representing the fractional change in proper area $\mathbf{A}(t)$ along the shell. Note that in first order hydrodynamics, the evolution equation for ρ_g is a second order PDE (second order ODE in spherical symmetry). If all the viscous transport coefficients are zero, it reduces to the first order, ideal equations [the term in the square brackets on the last line of (34)], and in that case, we directly integrate the latter for ρ_g . Recall that ρ and P in the metric and shell evolution equations are given by (23) and (24), respectively, and here

$$\begin{aligned}\mathcal{A} &= \tau_e \frac{F(\rho_g + p_g) + \dot{\rho}_g}{e^B \sqrt{1 - V^2}} \\ &= \tau_e \frac{3F\rho_g/2 + \dot{\rho}_g}{e^B \sqrt{1 - V^2}},\end{aligned}\quad (39)$$

$$\begin{aligned}\Pi &= \tau_p \frac{F(\rho_g + p_g - \zeta/\tau_p) + \dot{\rho}_g}{e^B \sqrt{1 - V^2}} \\ &= \tau_e \frac{F(3\rho_g/2 - 2\zeta/\tau_e) + \dot{\rho}_g}{2e^B \sqrt{1 - V^2}},\end{aligned}\quad (40)$$

where after the second equalities we have again substituted in $p_g = \rho_g/2, \tau_p = \tau_e/2$.

Note that (29) and (30) essentially contain the Israel junction conditions, but directly in terms of our metric

variables. In other words, demanding a coordinate system where the variables are continuous at the shell, but can have discontinuities in gradients, then it is only the latter terms above that can balance the delta function terms. These conditions give

$$\Delta C_r = -4\pi\rho e^B / \sqrt{1 - V^2}, \quad (41)$$

$$\Delta C_t = -V\Delta C_r, \quad (42)$$

$$\Delta B_r = 4\pi(\rho + 2P)e^B / \sqrt{1 - V^2}, \quad (43)$$

$$\Delta B_t = -V\Delta B_r, \quad (44)$$

where Δ refers to the jump in the respective quantity at the shell (one can check that the above expressions do coincide with the results computed directly using the Israel formalism.)

C. Constraint equations and initial data

Initial data for the metric evolution are subject to the usual constraint equations of general relativity. The tt component of the Einstein equations can be considered a constraint equation for C :

$$\begin{aligned}C'_r + \frac{3}{2}C'_t + C_r \left(\frac{3}{r} - B_r \right) - \frac{B_r}{r} \\ + 2\pi \left(\psi_r^2 + \xi_r^2 + \frac{2\rho e^B \delta(f)}{\sqrt{1 - V^2}} \right) + \frac{1 - \ell^2 r^2 e^{2B} - e^{2(B-C)}}{2r^2} \\ = \frac{C_t^2}{2} + B_t C_t - 2\pi(\psi_t^2 + \xi_t^2).\end{aligned}\quad (45)$$

We have placed time-dependent terms on the right-hand side, which for simplicity we will choose to be zero at the initial time (i.e., a moment of time symmetry). The tr component of the Einstein equations can then be considered a constraint equation for B :

$$\begin{aligned}\dot{C}_r + C_t \left(C_r - B_r + \frac{1}{r} \right) - B_t \left(C_r + \frac{1}{r} \right) \\ + 4\pi \left(\xi\Pi - \frac{V\rho e^B \delta(f)}{\sqrt{1 - V^2}} \right) = 0.\end{aligned}\quad (46)$$

Interestingly, at a moment of time symmetry, this is trivially satisfied, and B is arbitrary. At first glance, then, a simple choice is $B = \text{const.}$ (with an appropriate jump at the shell location); however, then the evolution equation implies there will be dynamics in B , even for a static shell. Instead then, we will use the evolution equation with all time derivatives set to zero to define our choice for $B(r, t = 0)$, as then the static case will be reflected as such in the solution. Specifically, we will solve the following for $B(r, t = 0)$:

$$B'_r - 4\pi(\rho + 2P)e^{2B}\delta(f)\frac{dr}{ds} + 4\pi(\xi_r^2 + \psi_r^2) - C_r^2 - \frac{2C_r}{r} - \frac{1 - e^{2(B-C)}}{r^2} = 0. \quad (47)$$

For the shell, a moment of time symmetry requires $V(t=0) = 0$, but the initial position and matter energy densities are arbitrary. For the latter, we will choose initial conditions to give a static shell when unperturbed, initializing the matter components following Ref. [3]. For the scalar fields, we set $\psi_t(r, t=0) = 0 = \xi_t(r, t=0)$ and freely choose $\psi_r(r, t=0), \xi_r(r, t=0)$, with the particular profiles discussed in Sec. VA 3.

D. Boundary conditions

For the inner boundary (origin of the AdS region), one can impose regularity through l'Hôpital's rule and requiring $C = C_0(t) + C_2(t)r^2$, and similarly for B and ψ (ξ does not extend into the interior). With this, the Einstein equations require $B_0(t) = C_0(t)$, together with the following conditions at $r = 0$:

$$\dot{C}_t - 6C'_r + B'_r = -e^{2B}\ell^2 - 2C_t^2, \quad (48)$$

$$\dot{B}_t - 2B'_r + 3C'_r = -4\pi\psi_t^2 + C_t^2, \quad (49)$$

$$\dot{\psi}_t - 3\psi'_r = -2\psi_t C_t. \quad (50)$$

For the outer boundary (in the AF region), one can use maximally dissipative boundary conditions (e.g., Ref. [17]). For instance, for the scalar field Ψ , its equation of motion when written in first order form (with $\Pi \equiv \Psi_{,t}$, $\Phi = \Psi_{,r}$) is given by

$$\dot{\Pi} = \Phi' + R_\Pi, \quad (51)$$

$$\dot{\Phi} = \Pi' + R_\Phi, \quad (52)$$

with R_Π, R_Φ the remaining terms of the corresponding equations not belonging to the principal part. The incoming (outgoing mode) at $r = R_{\text{out}}$ is $\Pi + \Phi$ ($\Pi - \Phi$). Maximally dissipative boundary conditions define incoming mode(s) as related to (and bounded by) the outgoing ones. For simplicity, we can do this at the level of the time derivatives of the modes; that is,

$$\dot{\Pi} + \dot{\Phi} = a(-(\Pi' - \Phi') + R_\Pi - R_\Phi), \quad (53)$$

$$\dot{\Pi} - \dot{\Phi} = -(\Pi' - \Phi') + R_\Pi - R_\Phi. \quad (54)$$

The first line states that the incoming mode is proportional (with proportionality constant a) to the outgoing mode. If $|a| < 1$, the condition is said to be maximally dissipative,

with $a = 0$ describing purely outgoing modes. The special case $|a| = 1$ corresponds to the reflecting case.

Now, solving for the time derivatives in (53) and (54), we derive what we should impose at the outer boundary point $r = R_{\text{out}}$:

$$\dot{\Pi} = \frac{(a+1)}{2}(-(\Pi' - \Phi') + R_\Pi - R_\Phi), \quad (55)$$

$$\dot{\Phi} = \frac{(1-a)}{2}((\Pi' - \Phi') - R_\Pi + R_\Phi). \quad (56)$$

In the code, we implement the above with $a = 0$ for the scalar field. For simplicity, we do the same with the metric variables, as they also obey wave equations. However, such maximally dissipative conditions are not fully consistent with the constraints, introducing an error that scales as $1/R_{\text{out}}$. To mitigate this problem, as described in Appendix C, we control the mapping between radial and code coordinates to push the outer boundary to be out of causal contact with the bubble for the duration of a given simulation.

E. Simplified shell dynamics with an external source

As discussed above, one of our goals motivating the particular choice of metric, coordinate conditions, etc., is to have a scheme that could eventually be generalized beyond spherical symmetry. Also, before taking on such an endeavor, we want to get some indication on how a gravitational wave might interact with the bubble, using a scalar field that can freely propagate across the bubble as a proxy for a gravitational wave. However, even in spherical symmetry, with these particular choices, there are various complications that arise, discussed in the Sec. VIB, that make it challenging to extract useful results on the physics of black bubbles in the large mass limit of interest. Here, then, we introduce a simplified model that allows us to explore black bubble stability in this regime, but it is only applicable to spherically symmetric systems and cannot model interaction with a bulk scalar field.

For this simplified model of the black bubble, consider a shell enclosing an AdS spacetime, with a Schwarzschild exterior that can contain unspecified matter. Here, we parametrize all shell quantities with proper time τ on the shell. We will model interaction with the exterior matter via a flux function $J_U(\tau)$. We also only consider a vacuum AdS interior, though in the linear analysis in Appendix B, we will allow a small internal mass to model some prior interaction that led to interior energy.

Thanks to spherical symmetry, we can solve such a model by integrating the Einstein and shell fluid equations purely at the shell location, making sure we self-consistently incorporate the backreaction of the external flux on the gravitational mass of the bubble. A straightforward way to compute the latter is to assume the external flux is coming from the scalar field ξ as in the full spacetime

model, and imposing the Einstein equations for this system just exterior to the shell, then taking the limit onto the shell (again, keeping the interior spacetime fixed). The effect of the scalar field can then simply be modeled as some freely specifiable $J_U(\tau) = -\xi_S(\tau)\xi_U(\tau)$; i.e., we do not need to know what particular external scalar field profile would be needed to lead to such a flux at the shell.

We impose the following ansatz for the spacetime:

$$ds^2 = -g(t, r)dt^2 + \frac{dr^2}{f(r, t)} + r^2 d\Omega^2. \quad (57)$$

Exterior to the shell, we set $f(r, t) = 1 - 2m(t, r)/r$, so $m(t, r = R)$ will represent the exterior Schwarzschild mass of the spacetime. We still have coordinate freedom with this ansatz to rescale t by an arbitrary function of itself and do so to impose $g(t, r = R) = f(t, r = R)$; i.e., evaluated at the shell, the exterior metric looks exactly like the Schwarzschild solution but with a time-dependent mass. Interior to the shell, we use the following static form for the AdS spacetime: $f(r) = g(r) = 1 + r^2\ell^2/3$. Below, metric quantities that are discontinuous across the shell are labeled with a subscript L when evaluated just to the left (interior) of the shell and with a subscript R just to the right (exterior) of the shell.

In this section, we will use the overdot to denote change with respect to proper time, e.g., $\dot{f} \equiv df(\tau)/d\tau$. With that notation, the evolution equations for the shell, its internal energy components, and $m(\tau)$ are

$$\dot{R} = V, \quad (58)$$

$$\begin{aligned} \dot{V} &= Q_L Q_R \left[\frac{2P}{\rho R} + \frac{1}{Q_L + Q_R} \left(\ell^2 \left[\frac{1}{4\pi\rho} - \frac{R}{2Q_L} \right] \right. \right. \\ &\quad \left. \left. - (\xi_S^2 + \xi_U^2) \left[\frac{2\pi R}{Q_R} + \frac{1}{\rho} \right] \right) \right] \\ &\quad + \frac{Q_L Q_R - 1 - V^2}{2R}, \\ &= \frac{R\ell^2 Q_R - 4\pi Q_L [R(\xi_S^2 + \xi_U^2) - 4P Q_R]}{2(Q_L - Q_R)} \end{aligned} \quad (59)$$

$$+ \frac{Q_L Q_R - 1 - V^2}{2R}, \quad (60)$$

$$\begin{aligned} \dot{\rho}_g &= -\frac{3\rho_g(R\dot{V} + V^2)}{R^2} - \frac{5V}{R}\dot{\rho}_g - \frac{\tau_p}{\tau_e} \left[\frac{2V}{R^2} (3V\rho_g + \dot{\rho}_g R) \right] \\ &\quad - \frac{1}{\tau_e} \left[(\tau_e + 1) \left(\frac{3V}{R} \rho_g + \dot{\rho}_g \right) - \frac{4\zeta V^2}{R^2} - j - \xi_U \xi_S \right], \end{aligned} \quad (61)$$

$$\dot{\rho}_s = -\frac{4V\rho_s}{R}, \quad (62)$$

$$\dot{\rho}_\tau = -j, \quad (63)$$

$$\dot{m} = \frac{4\pi R^2 Q_R (Q_R \xi_U - V \xi_S)(Q_R \xi_S - V \xi_U)}{f_R}, \quad (64)$$

where $f_R \equiv 1 - 2m(\tau)/R(\tau)$, $f_L \equiv 1 + R(\tau)^2\ell^2/3$, $Q_R \equiv \sqrt{f_R + V^2}$, $Q_L \equiv \sqrt{f_L + V^2}$, and

$$P = p_g + p_\tau + p_s + \tau_p \left[\dot{\rho}_g + \frac{2V(\rho_g + p_g)}{R} \right] - \frac{2V\zeta}{R}, \quad (65)$$

$$\rho = \rho_g + \rho_\tau + \rho_s + \tau_e \left[\dot{\rho}_g + \frac{2V(\rho_g + p_g)}{R} \right]. \quad (66)$$

The first equation for \dot{V} (59) stems from (22), and for reference below that in (60), we also include a form coming directly from the junction condition proportional to the net pressure (or equivalently eliminating ρ from the previous equation using the junction condition proportional to ρ). Again, the external source functions $\xi_U(\tau)$ and $\xi_S(\tau)$ can be considered freely specifiable; setting $\xi_U(\tau) = \xi_S(\tau)$ models the perfectly absorbing conditions.

For reference, as this will be needed for the flux j as described in Sec. IV, the exterior proper acceleration is

$$a_R = \frac{4\pi R^2 (\xi_U^2 + \xi_S^2) + 2\dot{V}R + 1 - f_R}{2Q_R R}, \quad (67)$$

where gradients of f and g appearing in its definition (25) have been eliminated using the Einstein equations.

F. Simplified dissipation

In the above equation, for ρ_g (61), we have included all the three relevant transport coefficients, τ_e , τ_p , and ζ , which in general are all dependent on ρ_g (hence, τ) and need to be nonzero to give a well-defined, hyperbolic theory. However, experimentation suggested τ_e , τ_p have little effect on the dynamics of the bubble. This can be understood by rewriting (61) as follows. Let $\mathcal{I} \equiv 2V(\rho_g + p_g)/R + \dot{\rho}_g$; i.e., $\mathcal{I} = 0$ is just the flux-free perfect fluid equation of motion. Then, in terms of \mathcal{I} , Eq. (61) becomes

$$\dot{\mathcal{I}} = -\mathcal{I} \left[\frac{\dot{\tau}_e + 1}{\tau_e} + \frac{2V}{R} \left(1 + \frac{\tau_p}{\tau_e} \right) \right] + \frac{4\zeta V^2}{\tau_e R^2} + \frac{j + \xi_U \xi_S}{\tau_e}. \quad (68)$$

This suggests that in spherical symmetry the parameters τ_e , τ_p essentially only control return to hydrodynamic evolution when starting from beyond-ideal conditions, i.e., ignoring the fluxes, if $\zeta = 0$ as with a conformal fluid, and we begin in equilibrium where $\mathcal{I} = 0$, then \mathcal{I} will remain zero for all

time, and ρ_g will always behave like an ideal fluid. The ζ term, being proportional to V^2 , becomes important with nonlinear perturbations, and since it is always positive, it is consistent with the intuition that this must come from dissipation removing kinetic energy from the motion of the bubble and depositing it in the gas. This is likewise consistent with the equation of motion for the bubble (59): if $\mathcal{I} = 0$, the τ_e, τ_p terms drop out from the expressions for the net pressure and energy density (65)–(66), and ζ controls the damping of the shell

$$\dot{V} \approx -V \frac{4\zeta Q_L Q_R}{R^2 \rho} + \dots, \quad (69)$$

where ... denotes terms that do not depend on any of the dissipation parameters.

Motivated by these observations, we set $\tau_e = \tau_p = 0$ [starting from (61), one needs to first multiply by τ_e , then take the limit]. With that, Eq. (61) becomes

$$\dot{\rho}_g = -\frac{3V}{R} \rho_g + \frac{4\zeta V^2}{R^2} + j + \xi_U \xi_S, \quad (70)$$

with

$$P = \frac{\rho_g}{2} - \rho_\tau + \rho_s - \frac{2V\zeta}{R}, \quad (71)$$

$$\rho = \rho_g + \rho_\tau + \rho_s. \quad (72)$$

Note that it would be trivial to add ζ -dissipation to the other shell components (with their sum then appearing in the expression for P above), or to split the energy flux $\xi_U \xi_S$ in some prescribed manner to the other matter components.

IV. AdS BLACK BUBBLE MATTER

In the preceding sections, we have described all of the components of the black bubble we study here, with the exception of the key property essential for it to be an astrophysically viable compact object candidate: stability. This, in principle, is achieved via an appropriate choice of internal flux j between the gas and brane components. We begin by reviewing the original suggestion for this given in Ref. [3], then describe its shortcoming and novel suggestions to overcome it.

As already mentioned, the shell is composed of three constituents, a brane with EOS $p_\tau = -\rho_\tau$, a gas of massless particles with EOS $p_g = \rho_g/2$, and a stiff fluid with EOS $p_s = \rho_s$, which are required based on physical and kinematic grounds. Let us review how this can be motivated from string theory. Inside of the shell, there is an AdS space with a negative cosmological constant. The main idea behind this scenario is that spacetime is unstable against decay to an AdS space. Usually, such a decay is heavily suppressed, but when matter threatens to collapse and form

a black hole, the nucleation is enhanced for entropic reasons. If a bubble forms, the infalling matter can turn into massless open strings, attached to the shell, carrying an entropy close to the one carried by a genuine black hole. This is similar to what is argued to happen in the case of fuzzballs. From string theory, it is expected that the scales associated with the negative cosmological constant, as well as the tension of the brane, are high energy, certainly beyond what is presently accessible through accelerator experiments and possibly close to the Planck scale.

The positive energy of the brane is supposed to closely match the negative energy of the vacuum inside of the shell. The mass of the system is then carried by the matter on top of the shell. If the shell has a radius given by $\frac{9R_s}{8}$, where R_s is the Schwarzschild radius, then the Israel-Darmois junction conditions force matter to have the equation of state (EoS) of a gas of massless particles. This special radius is often referred to as the Buchdahl radius. Such a matter component, composed of massless open strings attached to the brane, is natural from a string theoretical point of view. In order for the gas to be able to carry an entropy comparable to the one of a black hole, the number of degrees of freedom needs to be large. This can be accomplished if the end points of the strings are supported, not by the 2+1-dimensional brane itself but by a huge number of lower-dimensional branes dissolved in it. The need for such dissolved branes can also be seen by examining the junction conditions. This is where the stiff gas enters.

In string theory, 4D supersymmetric black holes can be constructed using 3-branes wrapping internal 3-cycles. Such branes will be point like from the 4D spacetime point of view. As suggested in Ref. [3], black bubbles in 4D can be obtained as 3-branes polarized into a 5-brane, still wrapping the internal 3-cycles. This 5-brane can still carry 3-brane charges represented by magnetic fluxes inside of the 5-brane. Ignoring the internal three dimensions, this is captured by the Dirac-Born-Infeld (DBI) action given by

$$S = \int d^3\sigma T_2 \sqrt{-\det(h_{\mu\nu} + \mathcal{F}_{\mu\nu})}, \quad (73)$$

where $T_2 = \rho_\tau$ is the tension of the shell and $\mathcal{F}_{\mu\nu}$ is the magnetic flux inside of the brane. The flux is quantized, and the energy density is schematically given by $4\pi T_2 \sqrt{r^4 + N^2}$, where N is an integer counting the number of dissolved branes. Note that if we formally take the radius of the shell to zero, the contribution of the shell goes away, and the energy is dominated by the mass of the D-particles. For a large shell, the contribution from the magnetic flux will be suppressed and, as explained in Ref. [3], have an energy density of order N^2/r^4 with the equation of state of a stiff gas. On top of this, there are massless fluctuations of the gauge fields. The number of such modes is order N^2 , and they give rise to the ρ_g that will carry the entropy.

In this way, one can solve the junction conditions, at the Buchdahl radius, using components motivated from string theory. For this setup to be a viable alternative to an ordinary black hole, it is not enough to find a critical point; it must also be stable. Unfortunately, this is not the case unless there is nontrivial dynamics involving energy exchange between the various components. The challenge is to find out what kind of dynamics is necessary, and whether this is what to expect from string theory. An argument for how stability could be obtained, based on thermalization at the local Unruh temperature, is given in Ref. [3]. Let us elaborate a bit on the argument presented there.

The shell will be heated through a nonzero Unruh temperature from the outside due to its nonzero proper acceleration sitting at a constant radius in the Schwarzschild metric.⁶ (There will be no such heating from the inside AdS region since there is a threshold for the acceleration [18]). If the temperature of the shell is a bit lower than the Unruh temperature, the gas will absorb Unruh quanta. Each mode will act as a little antenna. Thus, the shell will absorb at a rate of $N^2 \times R^2 \times T^4$. Since $N \sim R$ and $T \sim 1/R$, the total power of absorption will be of order 1. That is, the gas can absorb a mass of order M in light crossing time R . This suggests a term $\frac{\dot{T}}{T} \rho_g$, with no further suppression, contributing to the source term j . The Unruh quanta are not real, so energy needs to be supplied from the system itself for them to be created. In our model, it is the tension of the brane that is reduced in order to power the increased energy density of the gas. Note that the probability for energy to radiate off the system into the surrounding space, reducing the total energy, is heavily suppressed. Heuristically, the rate would not be order 1 but reduced by a factor $1/N^2$ due to self-absorption into the other modes. The resulting loss of energy is therefore of the same order as Hawking radiation and can be ignored in our analysis. The fact that the large number of degrees of freedom make it so entropically favorable for energy to get stuck to the brane is the reason why the system can so closely mimic a black hole, i.e., appearing to external observers as a near perfect black body of similar size and temperature to that of the equivalent mass black hole.

When the area of the shell changes, the number of dissolved branes, N , needs to change. Their energies are subleading, but when N changes, one would expect that the massless perturbations of the gauge field need to change, too. These carry important amounts of energy, and therefore one expects a contribution of the form $F\rho_g$ to j .

⁶Note that if the shell were brought towards the horizon, the Unruh temperature would increase toward infinity. As observed from infinity, the temperature will, when the redshift is taken into account, approach the Hawking temperature T_H . The temperature of the Buchdahl shell will be slightly lower and given by $\frac{64}{81} T_H$.

We have thus argued, from a microscopic point of view, for the presence of the two terms in our ansatz for j : one proportional to changes in the temperature T and the other proportional to changes in the area F . In the specific model described next, these terms are parametrized by constants α and β , respectively. In Ref. [3], values for α and β consistent with a quasistatic approximation were considered. However, such an approximation is not relevant for any real physical process where the shell is perturbed by infalling matter. In the discussion that follows, we will perform a more careful analysis, constraining the parameters so that we obtain a self-stabilizing shell. We will also verify the results using numerical methods. Interestingly, the constraint we find has a very simple and suggestive form.

A. Specific flux model

The total energy density ρ and pressure P sourcing Einstein's equations at the bubble location are the sum of the distributional matter terms

$$\rho = \rho_g + \rho_s + \rho_\tau, \quad (74)$$

$$P = p_g + p_s + p_\tau = \frac{1}{2} \rho_g + \rho_s - \rho_\tau, \quad (75)$$

where we ignore here any viscous corrections \mathcal{A} and Π to these quantities. As mentioned, we will require that the gas has a thermal component at the instantaneous local Unruh temperature of an observer on, but *outside* the shell,

$$T = \frac{a_R}{2\pi}, \quad (76)$$

where the subscript $(\)_R$ denotes the quantity is evaluated to the right (outside) of the shell. The vectors u^a and s^a are the same vectors on either side of the shell, as are their coordinate representations in our coordinate system; however, their gradients orthogonal to the shell are generally discontinuous across it. and in particular, the magnitude of the 4-acceleration evaluated using the EKGH metric is

$$a \equiv \nabla_a u^b u^a s_b = \frac{B_r + VB_t + \dot{V}/(1-V^2)}{e^B \sqrt{1-V^2}}, \quad (77)$$

and from (44), one can see how a will jump across the shell.

The continuity equation (20) is only required to be satisfied by the net fluid quantities ρ and P , and it is up to us to specify any internal interactions between the fluid constituents. As discussed in the previous section, the brane will provide the energy for heating/cooling and any response to changes in the area of the shell. Since the stiff fluid component is subleading, we only consider a flux j between the brane and gas, leading to the individual continuity equations given in (34)–(36) and (61)–(63), which we repeat here for convenience (without dissipative terms),

$$\dot{\rho}_g = -(\rho_g + p_g)F + j = -\frac{3}{2}\rho_g F + j, \quad (78)$$

$$\dot{\rho}_\tau = -(\rho_\tau + p_\tau)F - j = -j, \quad (79)$$

$$\dot{\rho}_s = -(\rho_s + p_s)F = -2\rho_s F, \quad (80)$$

and recall F represents the fractional change in proper area along the shell trajectory (38).

1. Internal energy exchange and stability

To obtain guidance leading to a concrete prescription for the internal flux, we begin by assuming the gas component ρ_g is purely thermal, namely,

$$\rho_g \propto N^2 T^3, \quad (81)$$

$$p_g = \rho_g/2, \quad (82)$$

where again N is the number of particles. With the assumption that N is fixed,

$$\dot{\rho}_g = 3\rho_g \dot{T}/T. \quad (83)$$

The continuity equation (78) gives an evolution equation for ρ_g ; therefore, if there was no source j , then (83) would simply tell us how the temperature evolves. On the other hand, as discussed above, it is assumed that locally the brane can interact with the gas on timescales much smaller than any macroscopic dynamical timescale to always keep the temperature fixed at the Unruh temperature (76). In that case, the continuity equation can be viewed as the definition of the flux of energy j coming from the brane required to enforce this; i.e., we want

$$\dot{a}_R/a_R = \dot{T}/T, \quad (84)$$

which requires the flux to be

$$j \equiv 3\rho_g(\dot{a}_R/a_R + F/2). \quad (85)$$

The appearance of the term F , representing the fractional change in area as the shell moves (38), exactly cancels the ‘‘usual’’ response of energy density to such a change in area (78). This comes from us assuming that the internal interaction in the shell is entirely driven by changes in the local proper acceleration and moreover that the interaction forces (81) to always be satisfied. The quasistationary analysis given in Ref. [3] suggested this was adequate for stability of the black bubble. However, as we show in Appendixes A and B, Ref. [3] ignored a dynamical component to changes in the 4-acceleration that has a destabilizing effect. Motivated by this observation, and the string theory considerations discussed above, we propose the following modification of (85) to model a broader class of internal interaction,

$$j \equiv 3\rho_g(\alpha\dot{a}_R/a_R + \beta F/2). \quad (86)$$

Here, α is a constant controlling changes to the internal state of the shell in response to changes in the Unruh temperature, while β is a constant controlling corresponding changes when the material compresses ($F < 0$) or expands ($F > 0$). This model is clearly *ad hoc*, though at least can be used to illustrate what kind of internal flux may be needed to stabilize the black bubbles and serve as a guidepost for future investigation of bubble constructions within a self-consistent theory.

2. Alternative flux model

We can also consider the gas temperature does not instantaneously adjust to the local Unruh temperature $T_u = a_R/2\pi$ but instead relaxes to it on a characteristic timescale τ_u via

$$\dot{T} = \frac{1}{\tau_u} \left(\frac{a_R}{2\pi} - T \right). \quad (87)$$

Carrying this through a similar calculation as above, and again generalizing with parameters α and β , defines an alternative flux option given by

$$j \equiv 3\rho_g \left(\frac{\alpha}{\tau_u} \left(\frac{a_R}{2\pi T} - 1 \right) + \beta F/2 \right). \quad (88)$$

With this prescription for the flux, T is evolved as an independent variable.

V. IMPLEMENTATION SPECIFICS

With the goal of studying the dynamical behavior of the AdS black bubble and potential observable consequences, we wrote two different codes for an efficient exploration. These implement the EKGH system in Sec. VA, which we employ to assess the full spacetime dynamics, and the shell model in Sec. VB to efficiently scrutinize the bubble’s behavior.

A. Einstein-Klein-Gordon-hydrodynamic system

For the most part, our discretization and solution of the EKGH system outlined in Sec. III A is straightforward and follows standard finite difference techniques. Especially, for the PDEs away from the shell location, we use second order accurate stencils for spatial gradients, add Kreiss-Oliger style dissipation [19], and for the time integration use a second order accurate explicit Runge-Kutta (method of lines) scheme.

Special treatment is needed at the location of the shell, where, even with our choice of a continuous metric across it, there are discontinuities in gradients there; hence, finite difference methods are not applicable. As discussed before, in spherical symmetry, where there are no propagating

gravitational wave degrees of freedom, one can treat the shell location as a “boundary” of both the interior and exterior spacetime, connecting them via the Israel junction conditions. However, this is not possible in general, as the shell location is not a boundary of the spacetime, and gravitational waves can freely propagate across it. We therefore want to implement a scheme that can integrate the field equations self-consistently across singular surface layers. Here, we do so via a weak-form, finite volumed inspired strategy, described in Sec. VA 1. In spherical symmetry in our chosen coordinates, this allows the gauge waves present in the metric variables B and C to freely propagate across the shell location, as well as our ψ scalar field proxy for gravitational waves, without imposing any boundary conditions. For simplicity, we have only implemented this to first order accuracy at present; hence, even though everywhere else the discretization is second order accurate, we only expect global first order convergence in the continuum limit.

It would be complicated to perform these weak-form integrations over a layer that moved on the coordinate grid. Therefore, as described in Sec. VA 2, we define a separate spatial code coordinate x and dynamically adjust the mapping to the metric coordinate r so that the bubble location is always at a fixed x coordinate. Of course, this is easy to do in spherical symmetry, and one might worry that generalizing this would be very challenging. However, we note that much more sophisticated “dual frame” schemes have already been successfully implemented in binary black hole merger simulations in full 3 + 1 dimensions [20] (see also Ref. [21]). There, the black hole excision surfaces are kept at fixed code locations, and it should be possible to adapt those techniques to bubble spacetimes, at least prior to any bubble collisions.

Note that in spherical symmetry, one can also solve the constraint equations in lieu of one or both of the evolution equations during evolution, as effectively the scalar field drives all the nontrivial dynamics then. Empirically, we have found solving (46) for C instead of the evolution equation (29) makes it easier to achieve stable evolution near the origin. Solving constraints instead of evolution equations is not easy to generalize to spacetimes without any symmetry; however, here, the origin difficulties are entirely because of spherical symmetry and would not be present in, for example, a Cartesian based coordinate system.

In Sec. VA 3, we list particular initial conditions we use for the shell matter and scalar fields.

1. Weak form integration

Here, we outline the idea behind a weak-form integration, leaving the description of the particular stencil used in our implementation in the code to Appendix D.

Equations (29)–(32) are all quasilinear wave equations of the form

$$\dot{f}(t, r) - g'(t, r) + h(t, r) + \delta(r - R)S(t, r) = 0, \quad (89)$$

as would the full 3 + 1D Einstein equations in harmonic form be. As mentioned, we discretize this using standard finite difference methods everywhere except at the shell. At that surface, here the point $r = R$ (which for now we consider to be constant), we apply the following finite volume, weak-form discretization. First, multiply the equation by a test function $v(r)$ that only has support within a cell of width $2\Delta r$ about the shell ($v(r) = 0$ for $|r - R| \geq \Delta r$), and integrate over the spatial volume of the cell:

$$\int (\dot{f} - g' + h + \delta(r - R)S)v dr = 0. \quad (90)$$

For simplicity, let $v(R) = 1$, and integrate the gradient term by parts, $g'v = (gv)' - gv'$, giving

$$\int ([\dot{f} + h]v + gv')dr = -S(t, R). \quad (91)$$

This is an improvement to before, because we have both been able to evaluate the delta function and have shuffled the spatial gradient from g to v , the former of which has a step at $r = R$ (as it must so that its gradient can compensate for the delta function in the equation of motion). In other words, we are free to choose $v(r)$ to be sufficiently regular so that v' is finite within the cell; hence, gv' is well defined and simple to evaluate, whereas, before, $g'v$ was not.

If the shell moves, i.e., $R = R(t)$, the above equation becomes more complicated to regulate, since the time derivative $\dot{f}(t, r)$ in (89) is the partial of $f(t, r)$ with respect to t at constant r , not constant R . Hence, in a typical wave equation where g and f are related, even if there is no singular behavior in time variation tangent to the shell, discontinuities in gradients orthogonal to the shell get spread into both $(\dot{})$ and $(\dot{})$ discontinuities, as the t and r coordinates are not aligned with the τ and s coordinates tangent and orthogonal to the shell, respectively. There are several conceivable ways to deal with such a situation. One is to extend (90) to an integration over a spacetime volume. Another is to choose coordinates that reduce to (τ, s) along the world line of the shell. A third, that we have chosen to use, described in the next section, and detailing its consequences for the weak-form integration in Appendix D, is to introduce a map $x(t) \leftrightarrow r(t)$ between the metric r and code x coordinates such that the shell is always at a constant x and then perform the spatial integration (90) over a cell of width $2\Delta x$.

2. Mapping between radial metric and code coordinates

We represent the various fields in our EKGH system on a uniform mesh in a coordinate $x \in [0..x_{\text{out}}]$, with the following key properties:

- (i) $x(r = R(t), t) = R(0) \equiv x_0$ (the shell stays at a constant $x = x_0$)
- (ii) $x(r = 0, t) = 0$ ($x = 0$ maps to $r = 0$)
- (iii) $x(r = R_{\text{out}}, t) = x_{\text{out}}$ (the outer boundary is at a fixed r and x)
- (iv) $\partial x(r, t)/\partial r|_{r=R(t)} = 1$ (the map is at least once differentiable at the shell location, and dx and dr have the same scale there).

We use polynomial functions for the map; the particular expressions are not too enlightening, so we list them in Appendix C. Note that this is not a coordinate transformation; we still evolve the metric functions B and C (28) and their partials B_r , C_r and B_t , C_t with respect to r and t , respectively. Another way then to think of this map is as a nonuniform, time-dependent discretization of r . The map will break down if the shell moves too far from its initial position, though this is only a problem for unstable bubbles.

3. Initial data

Our typical initial conditions consist of a static black bubble enclosing empty AdS spacetime, and then some prescribed external pulse for either of $\psi(r, t = 0)$ or $\xi(r, t = 0)$ (with $\psi_i(r, t = 0) = \xi_i(r, t = 0)$) that will subsequently interact with the shell to perturb it (for unstable bubbles numerical truncation error by itself will “perturb” the shell, causing it to either accelerate outward or collapse to a black hole, but this is not controllable in that the “perturbation” converges away with resolution). Specifically, given a desired initial $R_0 = 9m_0/4$ for the bubble, we set the shell components following Ref. [3] as⁷

$$\rho_g(t = 0) = \frac{\ell R_0 + (\ell R_0 - \sqrt{3})\sqrt{1 + \ell^2 R_0^2/3}}{12\pi\ell R_0^2\sqrt{1 + \ell^2 R_0^2/3}}, \quad (92)$$

$$\rho_s(t = 0) = \frac{\sqrt{3}}{16\pi\ell R_0^2}, \quad (93)$$

$$\rho_\tau(t = 0) = \frac{4\ell^3 R_0^3 + 8\ell R_0 + (\sqrt{3} - 8\ell R_0)\sqrt{1 + \ell^2 R_0^2/3}}{48\pi\ell R_0^2\sqrt{1 + \ell^2 R_0^2/3}}. \quad (94)$$

We set

$$\xi(r, t = 0) = \frac{A_\xi}{(\Delta_\xi)^8} (r - (R_\xi - \Delta_\xi))^4 (r - (R_\xi + \Delta_\xi))^4, \quad (95)$$

$$R_\xi - \Delta_\xi < r < R_\xi + \Delta_\xi, \quad (95)$$

$$= 0 \text{ elsewhere}, \quad (96)$$

where A_ξ , R_ξ , Δ_ξ are constants, and similarly for $\psi(r, t = 0)$.

⁷Note that their analysis only gives a unique decomposition in the large mass (radius) limit, and there are several conceivable ways of extrapolating that to $m = 0$; Eqs. (92)–(94) are one particular possibility.

B. Simplified shell model

The ODE equations governing the shell model, Eqs. (58), (60), (62), (63), (64), and (70), can be integrated straightforwardly with the flux j (86) for the instantaneous adjustment to the Unruh’s temperature of the gas. If, on the other hand, we employ the alternative flux prescription, we augment the evolution equations with (87) and the flux given instead by (88). The resulting equations are integrated with a standard fourth order Runge-Kutta scheme. Initial data are given by the static black bubble described in Sec. VA 3, and we consider its interaction with a perturbation given by $\xi_S(\tau)$, $\xi_U(\tau)$. We define these sources via superposition of functions of the form

$$\xi_S(\tau) = \xi_U(\tau) = A_\xi (e^{-((\tau - \tau_\xi^a)/\sigma_\xi)^2} + e^{-((\tau - \tau_\xi^b)/\sigma_\xi)^2}). \quad (97)$$

Setting $\xi_S = \xi_U$ corresponds to the maximum rate of absorption of energy by the gas (70). Finally, as we employ this code to explore the large m regime, given the disparate length scales involved (bubble mass, perturbation value, and timescale of interest), we adopt quadruple precision.

VI. APPLICATIONS/DYNAMICS

To explore the stability of black bubbles in the large mass limit, we use the simplified model described in Secs. III E and V B. These results are presented in Sec. VI A. In Sec. VI B, we show some results from the full model described in Secs. III A and VA, focusing on issues that would need to be overcome going beyond spherical symmetry and results from scalar field evolution on a fixed bubble background.

A. Numerical results from the shell model

We now focus on the simplified model described in Sec. III E and investigate a couple of interesting cases with parameters guided by a linear stability analysis of the system (Appendix B).

We impart a perturbation of the form (97) to the shell, which effectively implies “hitting” it twice: the first at $\tau = \tau_\xi^a$ to take it away from the static solution and a second one at $\tau = \tau_\xi^b = 15\tau_\xi^a$ to further perturb the intermediate state before it achieves equilibrium (if stable). For each perturbation, we evolve with two choices for the parameters $\{\alpha, \beta\}$. The first (case A) uses the constants $\alpha = 0.4$ and $\beta = 0.1$. As we show, this yields stable bubbles, but their final equilibrium states are not at a new Buchdahl radius. For the second (case B) then, we also keep $\beta = -1/3$, but now set α via the mass dependent relationship (B29) that the linear analysis identified as being necessary to keep the asymptotic bubble’s radius at its Buchdahl value. We adopt the simpler viscous equations (70) with $\tau_e = \tau_p = 0$ and $\zeta = 0.1$, and when employing the alternative flux option, we adopt $\tau_u = 2 \times 10^{-6}m$. These values of ζ, τ_u are not

special; the former are sufficiently small to play only a secondary role in the dynamics, and the latter imply a short time for the gas temperature to approach its corresponding Unruh value and can be chosen up to 100 times larger and still give essentially the same qualitative behavior.⁸

Before illustrating the bubble's behavior when perturbed, we note that there is a maximum amplitude of the perturbing pulse (for reasonable choices of parameters $\{\tau_\xi^a, \sigma_\xi\}$) that if exceeded (some of) the equations become singular. This singular behavior takes place when $\xi_S \approx m^{-1}$, which induces $a_R \rightarrow 0$ and $\dot{m} \rightarrow 1$, suggesting the bubble's growth approaches the speed of light and the effectively classical description of the bubble's internal dynamics ceases to make sense. As reference, for a perturbation with $\sigma_\xi \simeq m$, the largest mass change one can achieve is of $\approx 12\%$ after the two interactions. In what follows, we restrict to slightly lower values to avoid this situation. We consider a bubble with initial mass $m = 5000$ and choose the amplitude of the perturbation such that, after two perturbing episodes, the net relative change of the mass is $\Delta m/m = 0.2 \times 10^{-n}$ with $n = 3..5$. To more clearly illustrate the asymptotic state of the solution and its agreement (or lack thereof) with a Buchdahl state, we normalize each plotted quantity either by the (instantaneous) value expected for a Buchdahl solution or by the initial value of that quantity. Further, we also normalize by the inverse of the relative change in mass to more clearly compare with different chosen amplitudes.

First, Fig. 1 shows the behavior of radius and gas density vs (τ/m) . For both curves, we normalize them with respect to the corresponding quantities evaluated for the equilibrium solution with mass corresponding to the bubble's instantaneous mass and also by the inverse of the relative mass change $(\Delta m/m)$. As can be appreciated from the figure, while the late-time solution for both cases is stationary, for case A, this does not correspond to a Buchdahl state. On the other hand, case B shows both quantities converging to zero (the Buchdahl state) linearly with Δm .

Further insights into the dynamical behavior can be observed in Fig. 2, which shows the gas entropy and the temperature (normalized by the initial temperature). The entropy shows a net increase from the initial state to the final stationary solution, but as the interaction with the perturbation takes place, it shows a transient nonmonotonic behavior. Comparing the net entropy change (which can be consistently defined as the initial and final states are stationary) indicates case B has a larger final entropy than case A. Quantitatively, we find the net change of entropy from the initial state to the final equilibrium one is $\Delta S \approx C_S S_{g0}(\Delta m/m)$ with

⁸Even larger values produce a solution which is quite sensitive to this choice; lower ones give the same behavior, but if significantly smaller lead to a stiff equation, requiring a more delicate numerical treatment.

$C_{S_A} \approx 0.85, C_{S_B} \approx 2$. Recalling the gas entropy is $S_g = \rho_g R^2 T^{-1}$ and that for a state consistent with Buchdahl $\rho_g \propto R^{-1}$ for large masses, the value obtained for C_{S_B} is the expected one for a Buchdahl state. We note in passing that one can choose values for $\{\alpha, \beta\}$ that guarantee a monotonic growth of gas entropy, but unreasonably large values of the dissipation parameter ζ would be required for stability. Finally, the temperature indeed shows the expected reduction in value as the bubble grows, exhibiting a transient behavior as the interactions take place. Its asymptotic value denotes a

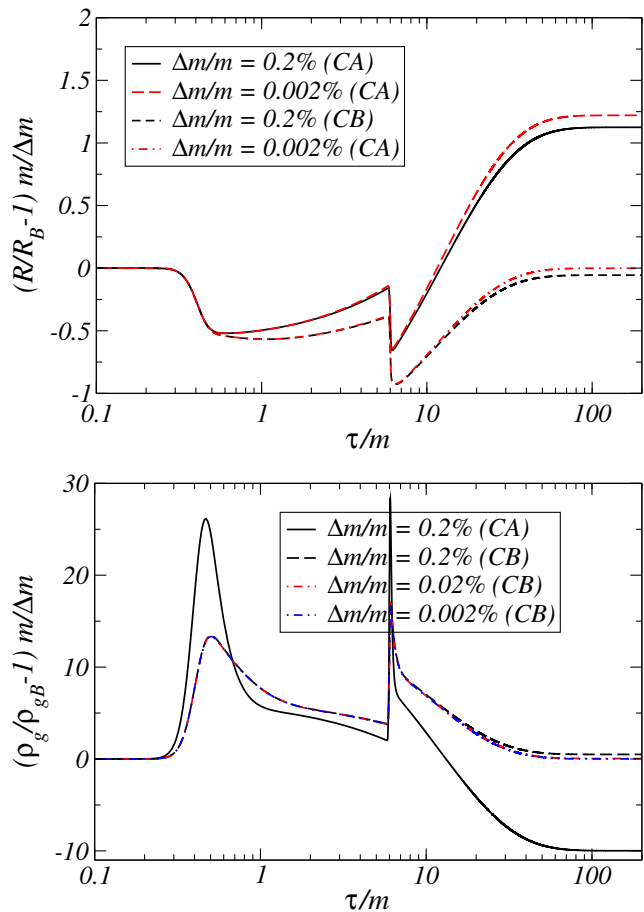


FIG. 1. Normalized radius (top panel) and gas density (bottom panel) from evolutions of a black bubble undergoing two distinct accretion episodes using the relaxation approach (88) (with $m = 5000$, $\ell = 1$, $\tau_u = 0.01$, and $\zeta = 0.1$). In the top panel, four solutions are presented, corresponding to relative mass changes of $\Delta m/m = 0.2, 0.002\%$ for each case. Case A asymptotes to a non-Buchdahl yet stationary solution, while case B converges to a Buchdahl state with a subleading correction that goes to zero with Δm . In the bottom panel, results corresponding to a mass change of $\Delta m/m = 0.2\%$ for case A and $\Delta m/m = 0.2, 0.02, 0.002\%$ for case B are shown. Case A asymptotes to a stationary solution distinct from the Buchdahl one, while case B converges to a Buchdahl state in a similar manner with Δm as the radius. (Note that both accretion episodes are of the same duration; that the second looks so abrupt is due to the logarithmic scale used for the time axis).

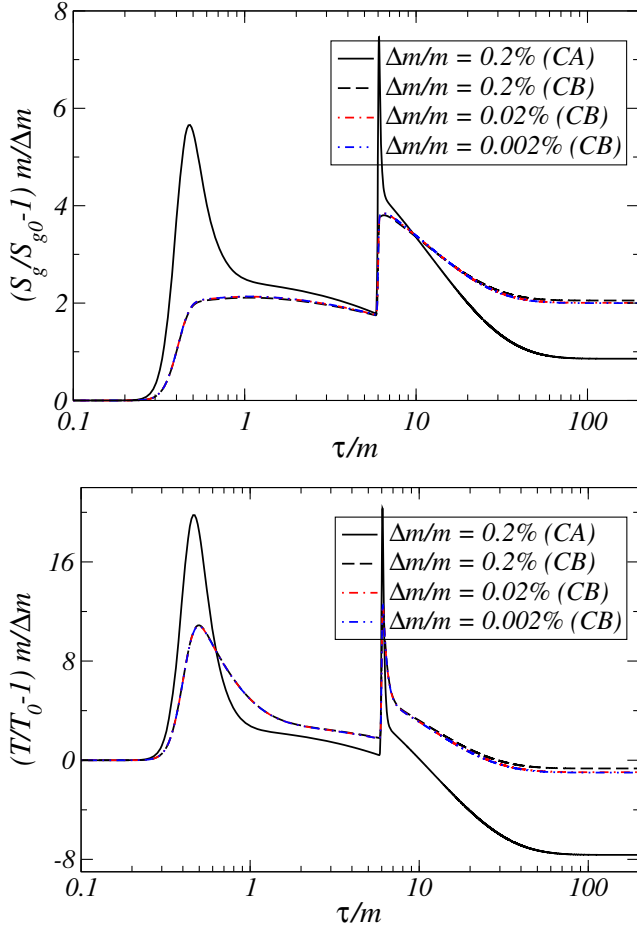


FIG. 2. Entropy (top panel) and temperature (bottom panel), normalized with respect to their initial values, from evolutions of a black bubble undergoing two distinct accretion episodes. Four runs are shown using the relaxation approach (88) (with $m = 5000$, $\ell = 1$, $\tau_u = 0.01$, and $\zeta = 0.1$) for case A (with a relative change of mass $\Delta m/m = 0.2\%$) and case B (with a relative change of mass $\Delta m/m = 0.2\%$, 0.02% , 0.002%).

change that can be approximated by $\Delta T \approx C_{T_i} T_0 (\Delta m/m)$, with $C_{T_A} \approx -7.5$, $C_{T_B} \approx -1$; the latter value corresponds to the expected one for a Buchdahl final state.

B. Numerical results from the Einstein-Klein-Gordon-hydrodynamic system

Since the ODE model can quickly and accurately study the stability of large black bubbles, we have, as demonstrated with some examples in the previous section, used that to map out black bubble matter properties that lead to stable configurations in spherical symmetry. Here, then, in the next two subsections, we show a couple of results from the EKGH system to illustrate some issues that would need to be addressed in future studies exploring black bubbles beyond spherical symmetry. In the last subsection, we explored evolution of scalar fields on a fixed black bubble background, which is possible with the EKGH code for

long timescales and up to modest values of the internal cosmological scale ℓ .

1. Accuracy and convergence

One of the issues limiting the EKGH code is related to accuracy: in this first attempt to model singular layers in a PDE code, we have sacrificed higher order convergence for the sake of simplicity. That would not have been much of an issue if the stability of black bubbles did not depend so

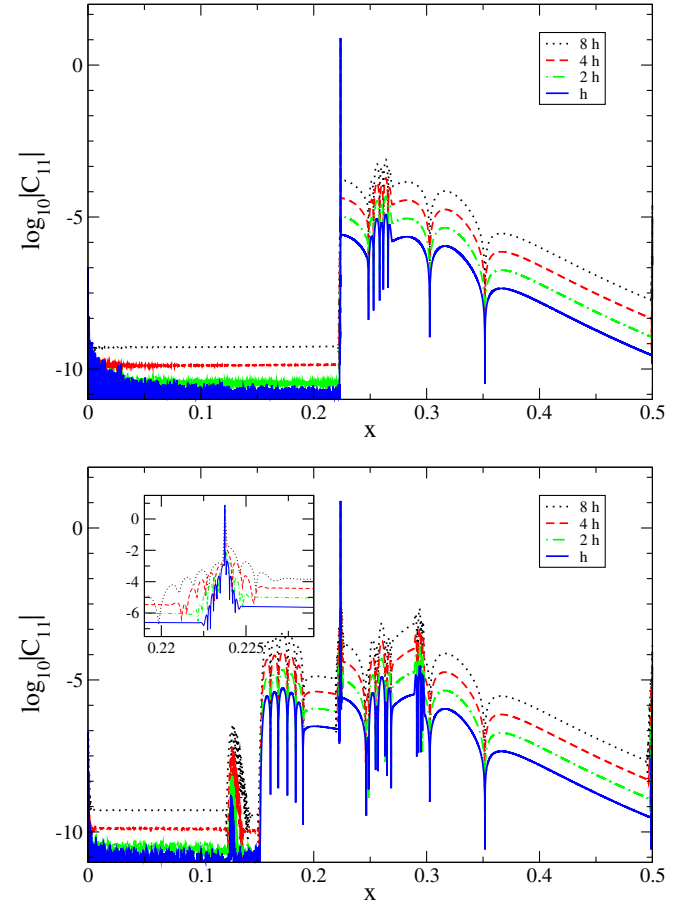


FIG. 3. The residual of (45) at $\tau/m = 0.01$ (top panel) and $\tau/m = 1.0$ (bottom panel), for an $m\ell = 0.1$ black bubble perturbed with a noninteracting scalar field ψ (using $\ell = 1$, $\alpha = 0.35$, $\beta = 0$, $\tau_u = 0.1$, $\zeta_0 = 1.0$, $\tau_e = \tau_p = 0$), where τ is proper time measured at the shell location. The finest resolution mesh spacing is $\Delta x = h = 0.5/32768$. The shell is at $x \sim 0.23$, corresponding (initially) to a proper radius $\bar{r} = 0.225m$, while the outer boundary $x = 0.5$ corresponds to a proper radius $126m$. At $\tau = 0$, the scalar field pulse is centered at $x = 0.27$ and has a coordinate width of 0.04 (95) and an amplitude so that it adds $\sim 0.002m$ to the mass of the spacetime (98). The initial data are time symmetric, so half falls into the bubble (corresponds to the second set of peaks out from the origin on the bottom panel—the smaller first peak is a transient emanating from the shell location at $t = 0$). The “noise” in the interior seems to be associated with the calculation reaching double-precision round-off error there.

sensitively on the scales in the problem. With a 1 + 1D code on a modern, single CPU machine we can evolve grids of up to 10^5 points for a similar number of time steps in about an hour of wall time. For small black bubbles, i.e., $m\ell \leq 1$, even with a code that is only first order convergent, we can achieve good accuracy over many shell light-crossing times. However, for reasons not entirely clear, though likely related to the mass amplification issue discussed in the following subsection, for $m\ell \geq 1$, the

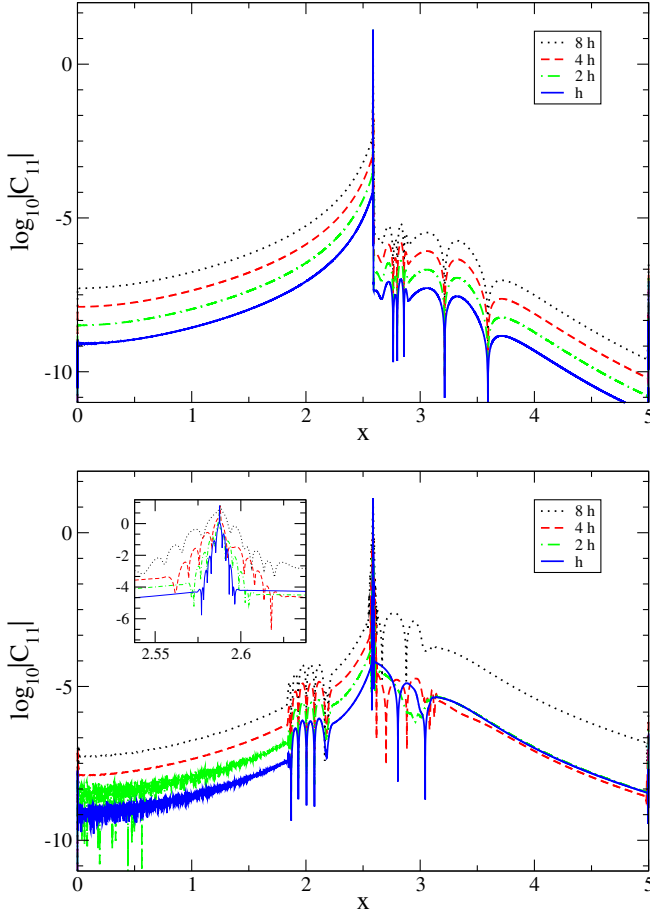


FIG. 4. The residual of (45) at $\tau/m = 0.01$ (top panel) and $\tau/m = 1.0$ (bottom panel), similar to the case shown in Fig. 3, but here for an $m\ell = 10$ black bubble, and the finest resolution mesh spacing is $\Delta x = h = 5.0/32768$. The shell is at $x \sim 2.5$, corresponding (initially) to a proper radius $\bar{r} = 22.5m$, while the outer boundary $x = 5.0$ corresponds to a proper radius $161m$. At $\tau = 0$, the scalar field pulse is centered at $x = 2.8$ and has a coordinate width of 0.4 (95) and an amplitude so that it adds $\sim 0.002m$ to the mass of the spacetime (98). In comparison to Fig. 3, notice the different magnitudes of the residuals. In particular, in this case, there is rapid growth of the residual exterior to the bubble with time, and moreover, it oscillates on a timescale of order τ/m —that the three higher resolutions seem to be the same at large radii is mostly coincidence as the oscillations happen to overlap at $\tau/m = 1.0$ (though there is also some deterioration of the rate of convergence, which does happen on such short timescales for these large mass cases).

truncation error at a given resolution rapidly increases with $m\ell$, so much so that by $m\ell \sim 10$ we cannot evolve for more than of order a light-crossing time at the highest resolutions before $O(1)$ errors are reached (in mass conservation, for example). Moreover, with certain flux parameters, there is a numerical instability that seems to set in for large $m\ell$ (or at least the growth rate depends on $m\ell$, and if present for smaller values is sufficiently mild that we have not noticed any lack of convergence then).

Figures 3 and 4 show examples of convergence for two different mass black bubbles, $m\ell = 0.1$ and $m\ell = 10$, respectively, perturbed with a noninteracting scalar field ψ (these are also the two outlier cases shown in Fig. 5). In both cases, after the ingoing component of the scalar field propagates across the shell, this perturbation results in a change of the mass aspect $m(r, t)$, defined via the following generalization of the Misner-Sharp mass [22],

$$1 - 2m/\bar{r} + \Theta(R - r)\ell^2\bar{r}^2/3 \equiv \nabla^b\bar{r}\nabla_b\bar{r}, \quad (98)$$

of $\sim 0.1\%$ evaluated just exterior to the bubble location $R(t)$ (the net initial energy of the scalar field is roughly twice this, with the other half propagating outward). In the above, $\bar{r}(r, t) \equiv \sqrt{\mathbf{A}(r, t)/4\pi}$ is an areal radius.

What is shown in Figs. 3 and 4 is residuals of the constraint C_{11} (45) (i.e., the left-hand side minus right-hand side of it) evaluated pointwise across the grid using centered, second order accurate finite difference stencils, at two times during the evolution. With our mapping of the shell to a constant location in $x = x_0$, we have also fixed that location to be at a vertex of the grid. Therefore, a

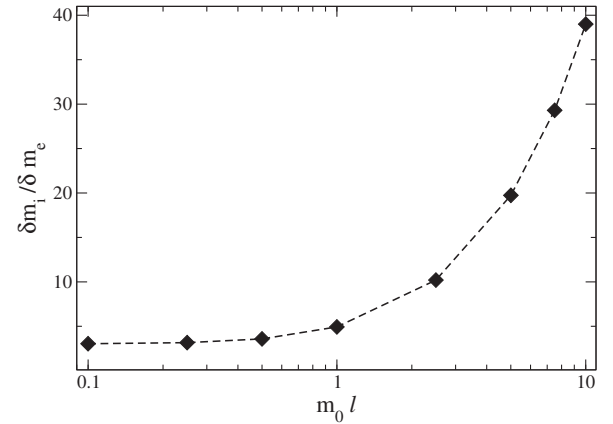


FIG. 5. The change in interior mass δm_i relative to the change measured exterior to the shell δm_e as a function of initial shell mass $m_0\ell$ (using $\ell = 1, \alpha = 0.35, \beta = 0, \tau_u = 0.1, \zeta_0 = 1.0, \tau_e = \tau_p = 0$). From convergence studies, estimated uncertainties in $\delta m_i/\delta m_e$ are less than 1% for all points (the dashed line between the points is simply to guide the eye). For all cases, the parameters of the perturbing scalar field were adjusted to give $\delta m_e \sim 0.001m_0$. For larger masses, $\delta m_i/\delta m_e$ grows linearly as a function of $m_0\ell$ (note that the figure has a logarithmic scale for the x axis).

consistent representation of the delta function appearing in (45) is to use the piecewise linear function that goes from 0 at $x_0 - \Delta x$ to $1/(2\Delta x)$ at x_0 and back to zero at $x + \Delta x$. Then, having evolved with a first order accurate finite volume integration about x_0 (see Appendix D), one only expects a consistent, convergent scheme to show convergence of a residual to zero in an integrated sense; specifically, $C_{11}(x_0, t)$ will evaluate to a finite function of time irrespective of resolution, though adjacent points around it should converge to zero first order in Δx . This can be seen in Figs. 3 and 4, though we do initially have second order convergence away from x_0 , and interestingly the region around $x = x_0$ that drops to first order with time grows quite slowly compared to the characteristic speed of the system.

The main point we want to illustrate with those figures is how much larger the truncation error is for large ($m\ell = 10$ in Fig. 4) vs small ($m\ell = 0.1$ in Fig. 3) mass bubbles. Note in particular the interior region, which is empty AdS to begin with, while in the exterior region by $\tau/m \sim 1$, the truncation error has grown to be of comparable magnitude for the $m\ell = 10$ case, and we are beginning to lose convergence there.

2. Interior energy

The second problem affecting the EKGH system evolutions is related to a physical issue, in that in the $m\ell \gg 1$ limit the bubble is very “close” to what would be the AdS boundary from the interior spaces’ perspective. One consequence of this is when we perturb the shell with a small, exterior noninteracting scalar field pulse; as it crosses the shell, it is very strongly “blueshifted.” So, in terms of a geometric mass (98), one can end up with a lot inside the shell. In fact, it is even possible to perturb the shell so that the interior mass ends up being larger than the asymptotic mass, and the shell acquires a negative gravitational mass. Such (and more modest cases) typically form black holes in the interior; considering quantum effects, presumably such states will eventually tunnel to a larger, encompassing black bubble.

To illustrate this interior geometric-mass amplification, in Fig. 5, we plot the change in interior mass (98) δm_i , measured just inside the shell, as a fraction of the change in exterior mass δm_e , measured just outside the shell. The $m_0\ell = 0.1, 10$ cases are from the same evolutions shown above with the convergence tests; the intermediate points are from similar runs with the perturbing scalar field parameters adjusted to also give $\delta m_e \sim 0.001m_0$ on a similar local timescale. Note that the linear analysis shows that for these parameters ($\alpha = 0.35, \beta = 0, \tau_u = 0.1, \zeta_0 = 1.0$) black bubbles with $m_0\ell \lesssim 0.5$ are unstable, and this is confirmed by the code, though for such relatively short interactions, $\delta m_i/\delta m_e$ does not depend on the flux parameters (we have not found a single set of parameters that give stable bubbles for both small and large masses).

Also, since no energy is directly exchanged with the shell matter, on these short timescales, ρ_g, ρ_τ , and ρ_s are roughly constant. The trend from the figure on the large mass side is that $\delta m_i/\delta m_e \approx m_0$ (e.g., for a similar 0.1% perturbation, cases with $m_0\ell \gtrsim 1000$ will give negative gravitational mass bubbles).

3. Gradual release of internal energy

For a rough estimate of the effect of internal energy, assuming it is not sufficient to collapse to a black hole nor trigger a quantum transition to a new black bubble configuration, here we evolve a free, noninteracting scalar field ψ on a black bubble background. With the PDE code, we can run such cases for many dynamical times, and up to modest values of ℓ of $O(10)$. The specific examples we show here choose an initial scalar field pulse of the form (95), though we use proper radius \bar{r} to define it to make for more meaningful comparisons varying ℓ (the relationship between r and \bar{r} in the light-metric (28) coordinates depends strongly on ℓ); we set $R_\psi = 3.5m$, $\Delta_\psi = m$ (and $m = 1$ in all cases).

The primary results are summarized in Figs. 6 and 7. First, as shown in Fig. 6, the scalar field that crosses into the bubble is partially trapped there, and leaks with time out, the more slowly the larger ℓ . Specifically, what is plotted there is the integrated energy density interior to the bubble

$$E_{\text{interior}}(\tau_0) \equiv \int_{\bar{r}=0}^{\bar{r}=9m/4} T_{ab} X^a n^b \sqrt{h} d^3x, \quad (99)$$

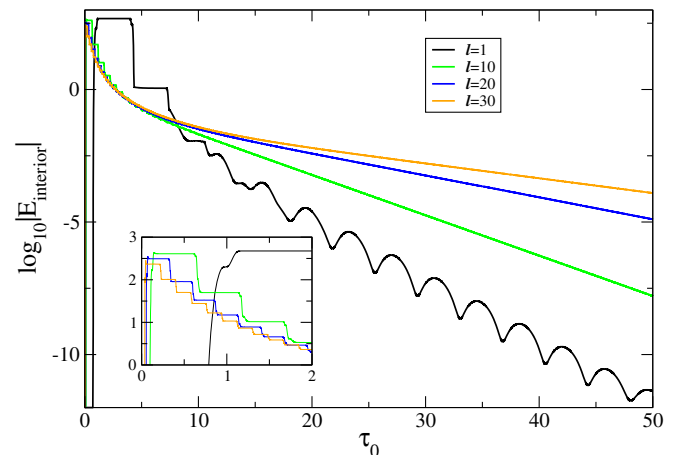


FIG. 6. Logarithm of the integrated energy (99) of the non-interacting scalar field ψ interior to the bubble, as a function of central ($\bar{r} = 0$) proper time τ_0 . These are all from runs *without* backreaction; i.e., the scalar field is simply propagating on the black bubble background. Runs using four different values for the cosmological constant scale ℓ are shown, each with $m = 1$, and an initial perturbation of characteristic width $\Delta\bar{r} = 1$ centered outside the bubble at a radius $3.5m$. The rate at which energy escapes clearly decreases with increasing ℓ .

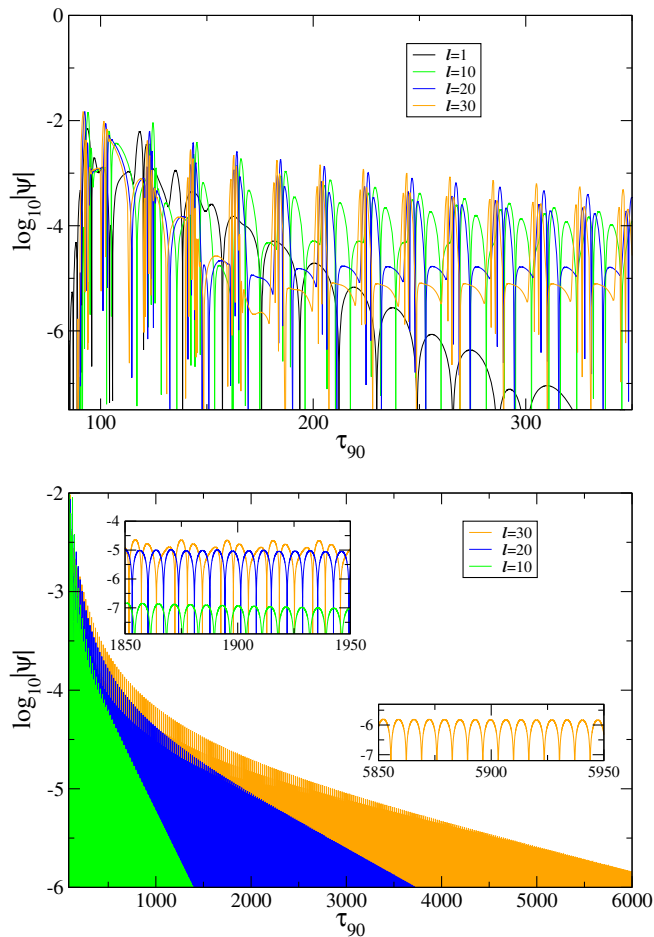


FIG. 7. The amplitude of the scalar field measured at $\bar{r} = 90m$ ($m = 1$) as a function of proper time τ_{90} for a static observer at this location, for the same cases shown in Fig. 6.

as a function of central proper time τ_0 , where $X^a = (\partial/\partial t)^a$ is the timelike Killing vector of the static background, n^a is the unit vector normal to $t = \text{const.}$ hypersurfaces, and h is the determinant of the corresponding spatial metric. On the background, a similar quantity would be conserved if the integral were carried out from $\bar{r} = 0$ to $\bar{r} = \infty$. The “blocky” nature of the curves at early times is associated with the light-crossing time of the pulse interior to the bubble, which decreases like $1/\ell$ with respect to the proper time at the origin of AdS. Initially, the pulse can be considered to be a superposition of many AdS scalar field normal modes; the higher harmonics leak out more quickly, gradually leaving behind the lower harmonics and a smoother late-time decay.

The reduction of energy within the AdS region can be understood straightforwardly following the analysis of, e.g., Ref. [23], and in Appendix E, we outline such a calculation. This shows that at late times when the fundamental mode dominates, and for large ℓ , one expects the interior energy to leak out via $\log E \sim \frac{2\pi}{m^2\ell} \tau_0$; this scaling with ℓ is consistent with the late-time slopes of the $\ell \geq 10$ curves shown in Fig. 6.

In Fig. 7, we show the imprint of this on the measured scalar radiation some distance outside the bubble. A few interesting features are apparent. Note the redshift between the oscillations with respect to central proper time depicted in Fig. 6 and the (near) asymptotic proper time in Fig. 7 (the same run time of $\tau_0 = 54m$ translates to $\tau_{90} \sim 2120m, 4160m, 6150m$ for the $\ell = 10, 20, 30$ cases, respectively, though the corresponding curves stop below the lower y axis limits of the figures). This means the observed rate of energy loss scales like $1/\ell^2$, as opposed to the $1/\ell$ measured with respect to interior central proper time (see Appendix E for more details). In terms of the externally observed frequency, the redshift also almost exactly compensates for the increasing internal oscillation frequency with ℓ , and the frequency observed at late times in the exterior is roughly independent of ℓ (see the insets on the bottom panel). Specifically, the late-time fundamental harmonic mode of a scalar field in AdS with frequency (relative to central proper time) $\omega_0 \sim \sqrt{3}\ell$ is observed at large radii redshifted to $\omega_\infty \sim 4/9/m$.

Finally, in Fig. 8, for comparison, we show two similar nonbackreacting runs, but now using the accreting scalar with perfectly absorbing boundary conditions. The first is the usual black bubble case at the Buchdahl radius, while for the second, the radius has been set to $\bar{r} = 2.001$ to

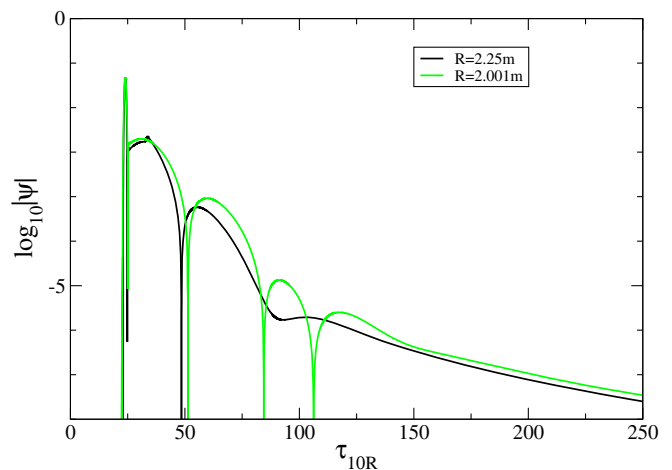


FIG. 8. The amplitude of the scalar field measured at $\bar{r} = 10R$ ($m = 1$) as a function of proper time there (τ_{10R}), for similar initial data as depicted for the runs in Fig. 7, but here with perfectly absorbing boundary conditions so that no scalar field enters the bubble (hence, ℓ is irrelevant). For the black curve, the bubble is at the canonical Buchdahl radius, while for the green, it is at $\bar{r} = 2.001m$, to mimic a black hole (and of course, such a bubble will be unstable if backreaction were included). Since the measurement radii are at slightly different locations, one curve was shifted in time to align the profiles at peak amplitude for ease of comparison. This would likewise affect the relative amplitudes, which has not been corrected for, though here we more want to emphasize the slight shift in frequency and number of quasi-normal oscillations visible before essentially the same power-law decay sets in.

mimic a black hole (we cannot set the boundary at exactly $\bar{r} = 2$, as the lightlike coordinates become singular then). The results are qualitatively similar, though they do differ in detail, suggesting that the early-time gravitational wave signal from black bubble formation will be similar to the black hole case, yet distinguishable with a precise enough measurement.

We discuss some of the potential observational consequences of this in the next section.

VII. CONCLUSIONS

In this work, we have taken first steps toward seriously considering the nonlinear classical dynamics of shell-like black hole mimickers (exotic compact objects). We formulated the problem within a fairly general framework that does not rely on symmetries of a single, isolated exotic compact object, though for simplicity in a concrete example, we restricted to spherical symmetry. Similarly, the novel techniques we introduced to implement this in a code were designed with application beyond spherical symmetry in mind.

The particular model exotic compact objects we studied are the AdS black bubbles of Ref. [3]. This model is motivated by string theory, and the initial investigations in Ref. [3] suggested they are stable—a crucial requirement for any astrophysically viable exotic compact object. An important physical ingredient for stable black bubbles is an internal interaction between the matter components of the bubble that causally reacts to external perturbations (such as accretion), keeping the bubble in an equilibrium configuration. We found here that the original quasistationary flux prescription of Ref. [3] was inadequate to maintain stability in dynamical situations and developed a two-parameter generalization of it. We identified regions of parameter space that do result in stable black bubbles, at least for sufficiently slow accretion. Moreover, within the space of stable bubbles, we were able to find parameters that guarantee (at the linear level for large black bubbles) that after a dynamical episode, the bubble relaxes to a new equilibrium black bubble; i.e., it sits at the Buchdahl radius corresponding to its new mass. Though we argued that the new parameters can be considered “natural,” we did not derive the new flux prescription from fundamental considerations, which would be an avenue for future research.

For rapid accretion, namely, when a sizeable fraction of the mass of the bubble accretes within of order the light-crossing time, we do find that otherwise stable bubbles can collapse to black holes. However, then, the internal fluxes take on values that suggest the evolution is outside the realm well described by the classical analysis. Likewise, anticipating what might happen when two black bubbles merge (assuming our stability results carry to nonspherical perturbations), a classical analysis should be valid during the inspiral up to a moment just before the actual merger. For the analog black hole case, in terms of local physics, a global apparent horizon suddenly forms that replaces the

apparent horizons of the two separate black holes. Similarly, there could be a quantum transition from one to two bubbles occurring before the two bubbles actually touch. Classically, one could attempt to model this in the same way by replacing the two bubbles with an encompassing single bubble. On the other hand, taking guidance from the way event horizons fuse together, one may be able to engineer the interaction between two bubbles so that at the instant of contact they similarly fuse into a single bubble. In the extreme mass ratio limit where no trapped surfaces would form as the two bubbles get close and fuse, the latter approach by itself could be an accurate approximation of the full quantum system (i.e., it may be that tunneling only occurs with high probability if a trapped surface would have otherwise formed).

Based on our results of scalar fields propagating on black bubble backgrounds, we can make some very speculative comments on observational consequences of black bubble formation or mergers (for a similar analysis related to gravastars, see [24,25]). First, regarding the gravitational wave analog where the scalar field is not absorbed by the bubble, this is unlikely to have observable consequences if $1/\ell$ is close to the Planck length L_p , or a similarly small microscopic scale. For then, as estimated in Appendix E, the internal energy is effectively trapped. On the other hand, one can take the perspective that we do not know what this scale is, and one can use black hole merger data to constrain it, or detect an unexpectedly large scale. This would be similar to the recent analysis in Ref. [26], in which the authors assumed there was an exotic compact object with purely reflecting boundary conditions some distance ϵ from the would-be Schwarzschild radius, and the absence of a long-lived, nearly monochromatic postmerger ringdown signal from GW150914 could constrain ϵ as a function of the ringdown timescale. Note that they do not propose that their exotic compact object can actually reflect gravitational waves (which would require matter that is bizarre even by the lax standards applied to exotic compact objects) but propose that, on long timescales, the passage through some interior geometry effectively looks like a reflection. A black bubble with a large $1/\ell$ would similarly produce a monochromatic late-time ringdown as illustrated in Sec. VIB, however at a frequency related to the Buchdahl radius as opposed to the Schwarzschild radius (and appropriately modified for rotation, as is necessary for GW150914 and was done in Ref. [26]). This suggests that black bubbles could offer an interesting counterexample to the conclusions given in Ref. [26], namely, that the absence of such a signal can be used to infer that the geometry outside the remnant of GW150914 must be close to that of Kerr down to some microscopic distance ϵ close to the horizon. In other words, for black bubbles, the absence of such a signal constrains the interior AdS scale but not macroscopic differences from Kerr in the exterior geometry. To constrain the latter would require understanding the prompt emission at the time of merger.

The comments about a late-time postmerger signal in the previous paragraph assumed external gravitational waves with wavelength of order the bubble radius propagate into the interior, and these essentially excite the lowest wavelength modes of the AdS interior. Such modes are very efficiently trapped there. However, as suggested by Eq. (E10), if there are internal quantum gravity processes that produce gravitational waves on small scales $1/j \sim 1/\ell$, they would leak out on observationally interesting time-scales even for $1/\ell \sim L_p$. Also, if the mass-amplification effect illustrated in Fig. 5 would classically cause a black hole to form in the interior, this will instead induce a tunneling event (or interior energy may induce tunneling to a new bubble regardless of classical black hole formation), and the arguments for the rate at which energy leaks out given in Appendix E would be invalid.

On another observational front, to explore how EHT images of supermassive black holes would change if they were supermassive black bubbles, it would be interesting to understand magnetohydrodynamic accretion from realistic models of accretion disks onto black bubbles. Backreaction is likely unimportant, and though black bubble spin would be, a good indication of whether the EHT could discriminate between black bubbles and black holes could be made using an exterior Schwarzschild background to begin with, assuming sufficient control of astrophysical processes are at hand. For the black bubble/magnetohydrodynamic interaction, a conservative approach would be to model it as perfectly absorbing, as with the scalar field case studied here.

There are many directions for future numerical studies of black bubbles. The most crucial would be to relax spherical symmetry to explore stability to nonradial perturbations and, if stable, accretion of angular momentum to uncover the rotating solutions. The fact that the bubble surface is within the photon sphere of the spacetime suggests there may be long timescale secular instabilities [27–29]. Classically, this might be analogous to the so-called weakly turbulent instability of AdS spacetime [30], which certainly is also relevant for the black bubble interior. If so, the consequence of the instability might “merely” be that trapped energy could eventually form small black bubbles that merge with the larger one. For rotating black bubbles, similar instabilities could be associated with the presence of an exterior ergoregion [31–33]. Also, it would be interesting to investigate whether in such cases there could be superradiant extraction of rotational energy, which may lead to similar observational signatures as the presence of ultralight particles around rotating black holes (see, e.g., Ref. [34]). Rotational energy may also be extracted if a Chandrasekhar-Friedmann-Schutz instability operates in fluid shells [35,36] (it is generic for rotating fluid stars in general relativity).

Regarding the physics of black bubbles, a next step would be to investigate whether the *ad hoc* flux model

prescribed here can be justified with more rigor. To fully capture the physics of the bubbles when they tunnel and merge will be challenging. It would require a significantly new conceptual understanding of tunneling in a time-dependent background, as well as the construction of methods capable of implementing this numerically. This would also be pertinent to understanding how soon after a merger the current model can be applied, which should adequately describe the late-time ringdown.

Last, we note that the AdS black bubbles we focused on are but one of many potential exotic compact object models. In that context, we hope our study, both in terms of the methods we have introduced and how we solved issues particular to black bubbles, can serve as a guide to further develop related exotic compact object models. Likewise, since the potential observable features indicated in this work can be traced back to key aspects of the model’s fundamental building blocks, other exotic compact objects with similar structure should exhibit the same qualitative observational characteristics. For instance, relating the late-time quasimonochromatic radiation frequency to a redshifted fundamental mode of the interior region, as well as connecting the amplitude of decay to interior energy loss, should be broadly applicable to any shell-like exotic compact object with a compact, leaky interior.

ACKNOWLEDGMENTS

We thank Will East, Anna Ijjas, Eric Poisson, and Paul Steinhardt for discussions. F. P., U. D., and L. L. thank the Simons Foundation for support to attend a workshop where this work was initiated. We acknowledge support from NSF under Grant No. PHY-1912171 (F. P.), the Simons Foundation (F. P.), NSERC (L. L.), and CIFAR (F. P. and L. L.). Research at Perimeter Institute is supported by the Government of Canada and by the Province of Ontario through the Ministry of Research, Innovation and Science.

APPENDIX A: DYNAMICAL EFFECTS ON PROPER ACCELERATION

The analysis of Ref. [3] found that a black bubble is stable to what are effectively quasistationary perturbations. Specifically, the authors considered the proper acceleration of an exterior, stationary observer,

$$a_s = \frac{f'}{2\sqrt{f}}, \quad (\text{A1})$$

with $f = 1 - 2m/\bar{r}$ in Schwarzschild coordinates and \bar{r} the areal radius, and here we use $' \equiv d/d\bar{r}$. The fractional change in acceleration that goes into the expression for the flux (85) was then defined to be $\dot{a}_s/a_s = Va'_s/a_s$, where $V = \dot{R}(\tau)$ is the shell velocity and $\dot{} \equiv d/d\tau$, with τ proper time along the shell trajectory.

However, in a dynamical situation, there are additional terms that appear in the expression for the 4-acceleration a_R , and it turns out these can counter the effect of the quasistationary term, in fact, so much so that adding the corresponding flux j can make the bubbles more unstable than without a flux. To see this, we evaluate (77) in Schwarzschild coordinates for a moving observer with unit 4-velocity $u^a = dx^a(\tau)/d\tau$,

$$a_R = \frac{1}{2} \frac{f' + 2A}{\sqrt{f + V^2}}, \quad (\text{A2})$$

with $A(\tau) = \dot{V}(\tau)$. This already hints at problems, as the acceleration can have an arbitrary sign irrespective of the motion of the shell, and the “wrong” sign will hinder the ability of a flux j based on (85) to return a perturbed shell to equilibrium. To see this more clearly, and that the general flux expression (86) with appropriate parameters could mitigate this problem, we compute (86) using (A2). The full expression is lengthy and somewhat obscure; to simplify, we evaluate it to leading order in V at the Buchdahl radius:

$$\begin{aligned} \left. \frac{j_m}{\rho_g} \right|_{\bar{R}=9m/4} &= \frac{243\alpha\bar{J}}{81\bar{A} + 16} \\ &- V \left[\frac{64(6\alpha - \beta) + 81(4[8\alpha - \beta] + 81\alpha\bar{A})\bar{A}}{3(81\bar{A} + 16)} \right] \\ &+ O(V^2), \end{aligned} \quad (\text{A3})$$

where we introduced the jerk $J(\tau) = \dot{A}(\tau)$ and rescaled the jerk and acceleration to given dimensionless quantities via $\bar{J} \equiv m^2 J$ and $\bar{A} \equiv mA$. The quasistationary case j_s is this expression with $\bar{A} = \bar{J} = 0$ and $\alpha = \beta = 1$,

$$\left. \frac{j_s m}{\rho_g} \right|_{\bar{r}=9m/4} = -\frac{20V}{3}. \quad (\text{A4})$$

Thus, for initial data where V is small, but A and J are zero, the analysis in Ref. [3] should hold, and the flux (A3) should start to counter the motion of the shell. However, this is not a generic perturbation, and perhaps a more “realistic” perturbation for a presumed stable shell would be the opposite case; i.e., we imagine a black bubble has formed and settled down to a stationary spacetime, and then we throw in an external perturbation. In that case, the first term in (A3) will dominate the flux, and this does not generically have the correct sign. Equation (A3) also suggests that a simple alternative stable prescription for triggering the internal fluxes is one based entirely on local changes to the area ($\beta \neq 0$) and not the Unruh temperature ($\alpha = 0$), if β is sufficiently negative.

APPENDIX B: LINEAR PERTURBATION ANALYSIS

In lieu of a full stability analysis, we will check whether stability is at least possible by seeking periodic solutions of the linearized equations for the simplified shell model presented in Sec. III E. We start with the following ansatz,

$$\begin{aligned} R(\tau) &= R_0 + \delta_R \cdot e^{i\omega\tau}, \\ \rho_i(\tau) &= \rho_{i0} + \delta_i \cdot e^{i\omega\tau}, \end{aligned} \quad (\text{B1})$$

where $R_0 = 9m/4$, ρ_{i0} are the equilibrium matter parameters for $i \in (g, s, \tau)$ and δ_R, δ_i are the magnitudes of a small perturbation. Here, we do not include any external fluxes but assume they were responsible for creating these perturbations.

Consider four options for the flux term j : $j = j_0 = 0$, $j = j_s$ from (85) with a_R given by the quasistationary case (A1), $j = j_d$ from the dynamical flux (86) with a_R given by the full expression (67), and $j = j_u$ using the alternative prescription for the dynamical flux (88) that explicitly introduces the temperature T and a corresponding relaxation to the Unruh temperature via (87). For the latter, we also adopt a similar ansatz for the temperature perturbation,

$$T(\tau) = T_0 + \delta_T \cdot e^{i\omega\tau}, \quad (\text{B2})$$

with $T_0 = 8/(27\pi m)$. For dissipation, we assume ζ is a constant ζ_0 . Plugging the above ansatz and flux options into the equations of motion, and expanding to linear order in (δ_R, δ_i) , a solution consists of constraints on the amplitudes of the matter (and temperature) perturbations δ_i (δT) in terms of the radial perturbation δ_R and a relation $\omega(m, \ell)$. These are more conveniently expressed in terms of dimensionless variables $\bar{m} = m\ell$, $\bar{\omega} = \omega/\ell$, $\bar{\tau}_u = \tau_u \ell$. We obtain for $j = 0$

$$\delta_{g,j_0} = -\delta_R \frac{4\ell^2}{81\pi\bar{m}^3} \left[(\bar{m} - 4\sqrt{3}/9) + \frac{4\bar{m}}{\sqrt{16 + 27\bar{m}^2}} \right], \quad (\text{B3})$$

$$\delta_{s,j_0} = -\delta_R \frac{16\sqrt{3}\ell^2}{729\pi\bar{m}^3}, \quad (\text{B4})$$

$$\delta_{\tau,j_0} = 0; \quad (\text{B5})$$

for $j = j_s$

$$\delta_{g,j_s} = 6\delta_{g,j_0}, \quad (\text{B6})$$

$$\delta_{s,j_s} = \delta_{s,j_0}, \quad (\text{B7})$$

$$\delta_{\tau,j_s} = -5\delta_{g,j_0}; \quad (\text{B8})$$

for $j = j_d$

$$\delta_{g,j_d} = \left[1 + 6\alpha - \beta + \frac{729\alpha\bar{\omega}^2\bar{m}^2}{64} \right] \delta_{g,j_0}, \quad (\text{B9})$$

$$\delta_{s,j_d} = \delta_{s,j_0}, \quad (\text{B10})$$

$$\delta_{\tau,j_d} = - \left[6\alpha - \beta + \frac{729\alpha\bar{\omega}^2\bar{m}^2}{64} \right] \delta_{g,j_0}; \quad (\text{B11})$$

and for $j = j_u$

$$\delta_{g,j_u} = \frac{\delta_{g,j_d} - i\bar{\tau}_u\bar{\omega}(\beta - 1)\delta_{g,j_0}}{1 + i\bar{\tau}_u\bar{\omega}}, \quad (\text{B12})$$

$$\delta_{s,j_u} = \delta_{s,j_0}, \quad (\text{B13})$$

$$\delta_{\tau,j_u} = \frac{\delta_{\tau,j_d} + i\bar{\tau}_u\bar{\omega}\beta\delta_{g,j_0}}{1 + i\bar{\tau}_u\bar{\omega}}, \quad (\text{B14})$$

$$\delta_T = -\delta_R \frac{(128 + 243\bar{m}^2\bar{\omega}^2)\ell^2}{162\pi\bar{m}^2(1 + i\bar{\tau}_u\bar{\omega})}. \quad (\text{B15})$$

The expressions for $\bar{\omega}$ are lengthy and not too illuminating by themselves, so for simplicity, we only show the more relevant large \bar{m} limit:

$$j = 0: \bar{\omega} \approx \frac{32\pi\zeta_0}{27\bar{m}} \left(i \pm i\sqrt{1 + 9/32/(\pi\zeta_0)^2} \right), \quad (\text{B16})$$

$$j = j_s: \bar{\omega} \approx \frac{32\pi\zeta_0}{27\bar{m}} \left(i \pm \sqrt{-1 + 27/(8\pi\zeta_0)^2} \right), \quad (\text{B17})$$

$$j = j_d, j_u: \bar{\omega} \approx \frac{128\pi\zeta_0}{27(4 - 9\alpha)\bar{m}} \cdot \left(i \pm \sqrt{-1 + 9(4 - 9\alpha)(6\alpha - \beta - 2)/(16\pi\zeta_0)^2} \right). \quad (\text{B18})$$

For $j = j_u$, there are three solutions if $\alpha \neq 0$; the first two are identical in the large mass limit to that of j_d (B18), with the third given by

$$j = j_u: \bar{\omega} \approx \frac{i(4 - 9\alpha)}{4\bar{\tau}_u} - \frac{i\alpha}{\bar{m}} \left[\frac{1}{\sqrt{3}\bar{\tau}_u} + \frac{64\pi\zeta_0}{3(4 - 9\alpha)} \right] \quad (\alpha \neq 0). \quad (\text{B19})$$

The zero flux ($j = 0$) and canonical ($\alpha = 1, \beta = 1$) dynamical flux $j_{d,u}$ cases always have at least one growing mode, while the quasistationary flux j_s is always damped.⁹ Various parameters can be found for the dynamical fluxes

⁹One could use the original quasistationary flux j_s and achieve linearly stable black bubbles, at least in spherical symmetry. However, this is a nonlocal flux; i.e., a fluid element on the bubble needing to respond to a perturbation cannot, using any local measurements of matter or spacetime properties, “know” what j_s should be. Moreover, it is unclear how (A1) could be extended beyond spherical symmetry even were one eager to adopt nonlocal physics.

$j_{d,u}$ to give damped systems. The third solution existing for the relaxation-based dynamical flux j_u is always stable for $\alpha < 4/9$, and \bar{m} sufficiently large that the second term in (B19) is subdominant.

1. Particular solution

In the analysis above, we did not include any external flux, assuming it was active prior to (say) $\tau = 0$ to set up the perturbation, after which one expects the solution to be given by some superposition of the above modes. In this regard, one thing missing from the above ansatz (B1) is the arbitrary small perturbations of the initial conditions that depend on the details of the prior external flux interaction. It is straightforward to show that including such general initial conditions requires adding a particular solution that simply shifts the final radius and temperature (for damped, stable cases) by constants dependent on these initial parameters but otherwise does not affect any of the linear modes.

Similarly, if the perturbation caused some matter to flow to the interior, and we model this as a small change δm_i to the interior mass, i.e., letting $f_L \equiv 1 + R(\tau)^2\ell^2/3 - 2\delta m_i/R(\tau)$, we can solve the linear equations if we add the following constant correction to R_0 in (B1)

$$R_0 \rightarrow R_0 + \frac{8}{81\bar{m}^2} \delta m_i + O(1/\bar{m}^4). \quad (\text{B20})$$

[A corresponding correction to T_0 scales like $O(1/\bar{m}^4)$]. This is a tiny correction to R_0 ; however, reversing the perspective, a perturbation that leaks energy into the interior resulting in a small change δR to the position of the bubble leads to a comparatively huge interior mass parameter $\propto \bar{m}^2\delta R$. It is not clear that we can combine this with the result shown in Fig. 5, in which the increase in interior mass comes from a scalar field interaction and $\delta m_i \propto \bar{m}\delta m_e$: for small perturbations, the scalar field will eventually escape, and for larger perturbations where a black hole forms to trap the scalar field, a linear analysis might not be warranted. Nevertheless, combining them for the case where an interior black hole does form, this suggests a change in radius (again for stable, damped cases) $\delta R \propto \delta m_e/\bar{m}$. In other words, this kind of perturbation, regardless of the flux parameters, will lead to a new (classical) equilibrium position that is not exactly at the new Buchdahl radius.

2. Impulse response

For stable black bubbles, to determine what (if any) internal matter fluxes are capable of maintaining the bubble at the Buchdahl radius after an accretion episode $\xi_U(\tau) = \xi_S(\tau) \equiv \xi(\tau)$, we consider the response of a bubble to an impulsive accretion event $\xi(\tau) = A\delta(\tau)$, with A a constant amplitude parameter. If flux parameters can be chosen to maintain such a condition for the impulsive response, then it should likewise be maintained at the linear

level for arbitrary accretion profiles $\xi(\tau)$. Mathematically, we can only make sense of a delta function source using the alternative flux model (87)–(88); for simplicity, we also only consider the simplified dissipation model (70).

The first step is to integrate Eqs. (58)–(60), (62)–(67), (70), and (87)–(88) about $\tau = 0$, with $\xi(\tau) = A\delta(\tau)$, to obtain the change in bubble properties from the prior static state $[R_0 = 9m_0/4, V_0 = 0, T_0 = 8/(27\pi m_0), \rho_{g0}, \rho_{s0}, \rho_{\tau 0}]$ (92)–(94), to the “initial” conditions $(R_i, m_i, V_i, T_i, \rho_{gi}, \rho_{si}, \rho_{\tau i})$ for the subsequent relaxation to the final equilibrium state $(R_f, m_f, V_f = 0, T_f, \rho_{gf}, \rho_{sf}, \rho_{\tau f})$ as $\tau \rightarrow \infty$. We find

$$R_i = R_0, \quad (\text{B21})$$

$$V_i = -\frac{9\pi Q_{L0}}{Q_{L0} - Q_{R0}} \bar{A}, \quad (\text{B22})$$

$$\bar{m}_i = \bar{m}_0 + \frac{27\pi \bar{m}}{4} \bar{A}, \quad (\text{B23})$$

$$\bar{T}_i = \bar{T}_0 - \frac{9}{2(Q_{L0} - Q_{R0}) \bar{\tau}_u} \bar{A}, \quad (\text{B24})$$

$$\rho_{gi} = \rho_{g0} + \left(\frac{\ell}{\bar{m}} - \frac{27\alpha \rho_{g0}}{2\bar{T}_0 \bar{\tau}_u (Q_{L0} - Q_{R0})} \right) \bar{A}, \quad (\text{B25})$$

$$\rho_{\tau i} = \rho_{\tau 0} + \frac{27\alpha \rho_{g0}}{2\bar{T}_0 \bar{\tau}_u (Q_{L0} - Q_{R0})} \bar{A}, \quad (\text{B26})$$

$$\rho_{si} = \rho_{s0}, \quad (\text{B27})$$

where $\bar{A} \equiv A\bar{m}/\ell$ and $\bar{T} \equiv T/\ell$. Next, we assume the solution for $\tau > 0$ can be written as a superposition of the three linear modes found in Appendix B, plus a relevant constant particular solution to fully (in addition to the amplitudes of the modes) account for the initial conditions. Assuming we choose parameters (α, β, τ_u) to give a stable bubble, plus some dissipation ζ_0 to give a static state at $\tau = \infty$, we can then straightforwardly read off the final state by evaluating this solution at $\tau = \infty$. Of particular relevance here is R_f/m_f , which in the large mass limit we find to be

$$\frac{R_f}{m_f} = \frac{3(15\alpha - 4)/4 - 4\sqrt{3}/(9\bar{m})}{6\alpha - \beta - 2} + O(\bar{m}^{-2}). \quad (\text{B28})$$

The linear mode analysis *assumed* what we want, namely, that $R_f/m_f = 9/4$, so for consistency here, this becomes a constraint:

$$\alpha = 2/3 + \beta - \frac{16\sqrt{3}}{81\bar{m}} + O(\bar{m}^{-2}). \quad (\text{B29})$$

Intriguingly, this can be expressed as

$$\alpha = \beta + \rho_{\tau 0} \frac{8\pi}{\ell\sqrt{3}} + O(\bar{m}^{-2}). \quad (\text{B30})$$

APPENDIX C: $x(r, t)$ map

We define the map between the metric r and code x coordinate as follows. First, define a quadratic map between x and an intermediate coordinate \hat{r} via

$$x(\hat{r}, t) = a(t)\hat{r} + b(t)\hat{r}^2, \quad \hat{r} \leq R(t) \quad (\text{C1})$$

$$= c(t) + d(t)\hat{r} + e(t)\hat{r}^2, \quad \hat{r} \geq R(t). \quad (\text{C2})$$

The functions $a(t)$, $b(t)$, $c(t)$, $d(t)$, and $e(t)$ are easily solved for by imposing the list of conditions given in Sec. VA 2 and that $x(\hat{r}, t = 0) = \hat{r}$. We then stretch the exterior part of the map to give $r(\hat{r})$,

$$r(\hat{r}) = \hat{r}, \quad \hat{r} \leq R(t) \quad (\text{C3})$$

$$= \hat{r} + \hat{r}_{\text{out}}(R_s - 1) \left[\frac{\hat{r} - R(t)}{\hat{r}_{\text{out}} - R(t)} \right]^3, \quad (\text{C4})$$

where the constant parameter R_s controls how far away in r we want the outer boundary location $\hat{r}_{\text{out}} = x_{\text{out}}$ to be. For the backreacting examples presented in Sec. VI B, we used $R_s = 10$, and we used $R_s = 40$ for the nonbackreacting cases.

APPENDIX D: WEAK-FORM INTEGRATION STENCIL

We integrate the evolution equations (29)–(31) about the location of the singular surface layer using the method outlined in Sec. VA 1. We use the map described in the previous section to keep it at a constant coordinate location x_0 and if necessary adjust the initial position of the shell to make sure x_0 coincides exactly with a vertex i_0 of the mesh. We use a two-cell-wide piecewise linear test function,

$$v(x) = 1 + \frac{(x - x_0)}{\Delta x}, \quad x_0 - \Delta x \leq x \leq x_0, \quad (\text{D1})$$

$$= 1 + \frac{(x_0 - x)}{\Delta x}, \quad x_0 \leq x \leq x_0 + \Delta x, \quad (\text{D2})$$

$$= 0, \text{ elsewhere,} \quad (\text{D3})$$

where Δx is the mesh spacing. Similarly, we decompose all metric and scalar field functions in a basis of piecewise linear functions in x , assuming the exact values are stored at grid vertices. For example,

$$f(x) = f_{i-1} \frac{x_i - x}{\Delta x} + f_i \frac{x - x_{i-1}}{\Delta x} \quad x_{i-1} \leq x \leq x_i, \quad (\text{D4})$$

where the notation f_i means $f(x = x_i)$, with $x_i \equiv i\Delta x$. For a quantity f that is discontinuous, hence multivalued at i_0 , we will use the notation f_L (f_R) to denote its value just to the left (right) of i_0 . We can then analytically integrate (91), arriving at an algebraic equation that we can solve for the time derivative of the quantity of interest at i_0 . Note that if one wanted to increase the accuracy of the scheme at the surface layer, one could do so by using higher degree polynomials (or other, smoother basis functions) to represent the fields and test function.

Before writing down the resultant stencil, we note a couple of technical complications to reach the equivalent of the final integral given in (91), related to our dual r, x

coordinate scheme. The first is we are integrating in x , so we need to include the Jacobian of the coordinate transformation in the integral (90) and carry it through the subsequent integration by parts. Second, our Runge-Kutta integration scheme requires $\partial f(x, t)/\partial t$ at fixed x , though all the time derivatives in (29)–(31) are at fixed r ; hence, we also need to transform between \dot{f} and $\partial f(x, t)/\partial t$ [recall our notation $\dot{f} \equiv \partial f(r, t)/\partial t$, $f' \equiv \partial f(r, t)/\partial r$].

With all that, our first order accurate finite volume form of (89), which we repeat here for reference,

$$\dot{f}(t, r) - g'(t, r) + h(t, r) + \delta(r - R)S(t, r) = 0, \quad (\text{D5})$$

can be written as

$$\begin{aligned} \frac{d}{dt}f_{i_0} = & -\frac{1}{4}[g' + f' \cdot r_t]_{i_0+1} + \frac{1}{4}[g' + f' \cdot r_t]_{i_0-1} - \frac{1}{4}[f \cdot r_{tr} + (f \cdot r_t + g)x'' \cdot r_x]_{i_0+1} \\ & + \frac{1}{4}[f \cdot r_{tr} + (f \cdot r_t + g)x'' \cdot r_x]_{i_0-1} - \frac{1}{2}(h_L + h_R) - \frac{1}{2}(f_L + f_R) \cdot r_{tr} \\ & - \frac{1}{2}[(f_L \cdot r_{t,i_0} + g_L) \cdot x''_L + (f_R \cdot r_{t,i_0} + g_R) \cdot x''_R] \cdot r_{x,i_0} \\ & + \frac{3}{4\Delta x}[(g_R - g_L + (f_R - f_L) \cdot r_t) \cdot x'_{i_0} + [(g + f \cdot r_t) \cdot x']_{i_0+1} \\ & - [(g + f \cdot r_t) \cdot x']_{i_0-1} - 2S_{i_0} \cdot x'_{i_0}], \end{aligned} \quad (\text{D6})$$

where $r_t \equiv \partial r(x, t)/\partial t$, $r_x \equiv \partial r(x, t)/\partial x$, $r_{tr} \equiv [\partial^2 r(x, t)/(\partial t \partial x)] \cdot \partial x(r, t)/\partial r$. This elevates to a second order accurate scheme when $S_{i_0} \rightarrow 0$, and all “L” values equal their “R” value neighbors.

APPENDIX E: RATE OF ENERGY LOSS FROM AdS INTERIOR

In lightlike coordinates, the line element for AdS is

$$ds^2 = \cos^{-2}(\ell r/\sqrt{3})(-dt^2 + dr^2) + 3/\ell^2 \tan^2(\ell r/\sqrt{3})d\Omega^2, \quad (\text{E1})$$

which we distinguish from the “standard coordinates” (r, R) , which give

$$ds^2 = -(1 + R^2\ell^2/3)dt^2 + (1 + R^2\ell^2/3)^{-1}dr^2 + R^2d\Omega^2. \quad (\text{E2})$$

General solutions to scalar field propagation in AdS in lightlike coordinates can be expressed as a superposition of modes given by

$$\begin{aligned} \Phi_j(t, x) = & d_j \cos(\omega_j \ell t/\sqrt{3}) \cos^3(\ell r/\sqrt{3}) \\ & \times {}_2F_1(-j, 3 + j, 3/2, \sin^2(\ell r/\sqrt{3})), \end{aligned} \quad (\text{E3})$$

with $\omega_j^2 = (3 + 2j)^2\ell^2/3$ and $d_j = 4\sqrt{(j+1)(j+2)}/\pi$ ($j \in 0, 1, \dots$). Such modes are orthonormal and complete as $\ell \rightarrow \infty$. For our regime of interest then, we can use this (quasi)basis, for large ℓ , to describe the exterior pulse once it enters the AdS region. In particular, we are interested in the reduction of (the interior) energy (E) within the AdS. To this end, we can make use of the analysis presented in Ref. [23] to reach the intuitive result of

$$E_{,t} = 4\pi(V_+^2 - V_-^2)R_\rho^2, \quad (\text{E4})$$

with $V_{+,-} = \pm \alpha u^a \partial_a \Phi + \alpha D$ the incoming (outgoing) modes of the solution at the outer boundary $r = R_\rho$; u^a is the unit timelike normal at R_ρ , $D = \gamma^{ij}n_i \partial_j \Phi$, and $\alpha = 1/\cos(\ell r/\sqrt{3})$. At such a boundary, the AdS region loses energy through V_- but does not gain energy through V_+ as little “comes back” from the exterior region. We can thus take it to zero, so energy is lost at a rate $E_{,t} = -4\pi V_-^2 R_\rho^2$. We can then replace Φ in terms of its normal modes; it is clear higher modes will reduce the energy more effectively than the lowest one ω_0 . Said

differently, energy supported by higher frequency modes leaks out at a faster rate out of the AdS region. The long-term behavior is given by the lowest mode, and the energy loss within one period of oscillation is, to leading order in $1/\ell$,

$$\Delta E \propto -A_0^2 \pi^2 \frac{1}{m^2 \ell^3} \quad (\text{E5})$$

(with A_0 the amplitude of the mode). We can then use a “quasiadiabatic” argument to say an amount of energy

$$\Delta E \propto -A_0^2 \pi^2 \frac{1}{m^2 \ell^2} \Delta T \quad (\text{E6})$$

is lost in the interior region over the period $\Delta T = (2\pi)/(\ell\sqrt{3})$. Now, the energy within the AdS region is $\propto A_0^2/\ell$, so $dE/dt \propto 2A_0/\ell dA_0/dt$, and we can use $\Delta E/\Delta T$ to approximate the left-hand side to arrive at

$$\frac{dA_0}{dt} \propto -\frac{\pi A_0}{m^2 \ell^2} \ell, \quad (\text{E7})$$

and so, $A_0(t) \approx \exp(-pt\ell)$ with

$$p \approx -\frac{\pi}{m^2 \ell^2}. \quad (\text{E8})$$

Thus, the energy decays as $E(t) \propto \exp(-2pt\ell)/\ell$, and so $\log E \approx -\frac{2\pi}{m^2 \ell^2} t$. Notice the above expression is with respect to time measured at the origin of AdS, which is related to the asymptotic time t_a by $t \approx t_a/(m\ell)$. Consequently, $\log E \approx -\frac{2\pi}{m^2 \ell^2} t_a$. This behavior is consistent with the results shown in Figs. 6 and 7. For reference, we can

now explore the associated timescale for this energy to leak out of AdS and become an “observable signature” in the asymptotically flat (AF) region. The timescale is given by $\tau_D \simeq m^3 \ell^2$; taking $\ell = 1/L$ with L a lengthscale and assuming $m = 10^q M_\odot$, one has

$$\tau_D = 10^{3q} (m/L)^2 \text{ s}. \quad (\text{E9})$$

For instance, for $L = L_{\text{Planck}} \simeq 10^{-35}$ m and $q = 1$, $\tau_D = 10^{53}$ s $\approx 10^{56} t_{\text{Hubble}}$. Requiring instead that $\tau_D \simeq t_{\text{Hubble}}$ or $\tau_D \simeq 1$ yr, L should be $\simeq 10^{-7}, 10^{-4}$ m, respectively.

As a last remark, we can employ a similar argument to explore what takes place at early times. When a pulse with a given frequency ω_{AF} in the AF region begins to fall in the AdS region, its frequency would be blueshifted to $\omega_i \simeq \omega_{\text{AF}} m \ell$ and would be supported, in terms of the AdS modes, by a spectra of (almost) normal frequencies given by $\omega_j = \pm(3 + 2j)\ell/\sqrt{3}$. Thus, the pulse would be described by the same modes in a way that is largely insensitive to the scale determined by ℓ . For a mode with index j , the above timescale estimate results in

$$\tau_D = 10^{3q} j^{-2} (m/L)^2 \text{ s}, \quad (\text{E10})$$

indicating the AdS could help potentially render microscopic j scales into significantly longer ones for higher values of j . Of course, this depends on the content of the pulse in the AF region. Rough estimates, however, imply not very high j 's are encountered with significant strength for the relatively simple frequency content of waves driven by a quasicircular merger.

-
- [1] O. Lunin and S. D. Mathur, AdS/CFT duality and the black hole information paradox, *Nucl. Phys.* **B623**, 342 (2002).
- [2] P. O. Mazur and E. Mottola, Gravitational condensate stars: An alternative to black holes, [arXiv:gr-qc/0109035](https://arxiv.org/abs/gr-qc/0109035).
- [3] U. H. Danielsson, G. Dibitetto, and S. Giri, Black holes as bubbles of AdS, *J. High Energy Phys.* **10** (2017) 171.
- [4] V. Cardoso and P. Pani, Testing the nature of dark compact objects: A status report, *Living Rev. Relativity* **22**, 4 (2019).
- [5] B. Abbott, R. Abbott, T. Abbott, S. Abraham, F. Acernese, K. Ackley, C. Adams, R. Adhikari, V. Adya, C. Affeldt *et al.*, GWTC-1: A Gravitational-Wave Transient Catalog of Compact Binary Mergers Observed by LIGO and VIRGO During the First and Second Observing Runs, *Phys. Rev. X* **9**, 031040 (2019).
- [6] T. L. S. (the Virgo Collaborations), GWTC-2.1: Deep extended catalog of compact binary coalescences observed by LIGO and VIRGO during the first half of the third observing run, [arXiv:2108.01045](https://arxiv.org/abs/2108.01045).
- [7] E. H. T. Collaboration, First M87 event horizon telescope results. I. The shadow of the supermassive black hole, *Astrophys. J. Lett.* **875**, L1 (2019).
- [8] U. Danielsson and S. Giri, Observational signatures from horizonless black shells imitating rotating black holes, *J. High Energy Phys.* **07** (2018) 070.
- [9] W. Israel, Singular hypersurfaces and thin shells in general relativity, *Nuovo Cimento B Serie* **44**, 1 (1966).
- [10] B. P. Abbott *et al.*, Observation of Gravitational Waves from a Binary Black Hole Merger, *Phys. Rev. Lett.* **116**, 061102 (2016).
- [11] R. Abbott *et al.*, GWTC-2: Compact Binary Coalescences Observed by LIGO and Virgo During the First Half of the Third Observing Run, *Phys. Rev. X* **11**, 021053 (2021).

- [12] K. Akiyama *et al.*, First M87 event horizon telescope results. I. The shadow of the supermassive black hole, *Astrophys. J. Lett.* **875**, L1 (2019).
- [13] F. S. Bemfica, M. M. Disconzi, and J. Noronha, General-relativistic viscous fluid dynamics, [arXiv:2009.11388](https://arxiv.org/abs/2009.11388).
- [14] F. S. Bemfica, M. M. Disconzi, and J. Noronha, Causality and existence of solutions of relativistic viscous fluid dynamics with gravity, *Phys. Rev. D* **98**, 104064 (2018).
- [15] P. Kovtun, First-order relativistic hydrodynamics is stable, *J. High Energy Phys.* **10** (2019) 034.
- [16] A. Pandya and F. Pretorius, Numerical exploration of first-order relativistic hydrodynamics, *Phys. Rev. D* **104**, 023015 (2021).
- [17] G. Calabrese, L. Lehner, O. Reula, O. Sarbach, and M. Tiglio, Summation by parts and dissipation for domains with excised regions, *Classical Quantum Gravity* **21**, 5735 (2004).
- [18] S. Deser and O. Levin, Accelerated detectors and temperature in (anti)-de Sitter spaces, *Classical Quantum Gravity* **14**, L163 (1997).
- [19] H. Kreiss and J. Olinger, *Methods for the Approximate Solution of Time Dependent Problems*, Global Atmospheric Research Programme (GARP): GARP Publication Series Vol. 10 (GARP Publication, 1973).
- [20] M. A. Scheel, H. P. Pfeiffer, L. Lindblom, L. E. Kidder, O. Rinne, and S. A. Teukolsky, Solving Einstein's equations with dual coordinate frames, *Phys. Rev. D* **74**, 104006 (2006).
- [21] D. Hilditch, Dual foliation formulations of general relativity, [arXiv:1509.02071](https://arxiv.org/abs/1509.02071).
- [22] C. W. Misner and D. H. Sharp, Relativistic equations for adiabatic, spherically symmetric gravitational collapse, *Phys. Rev.* **136**, B571 (1964).
- [23] G. Calabrese, L. Lehner, D. Neilsen, J. Pullin, O. Reula, O. Sarbach, and M. Tiglio, Novel finite-differencing techniques for numerical relativity: Application to black-hole excision, *Classical Quantum Gravity* **20**, L245 (2003).
- [24] P. Pani, E. Berti, V. Cardoso, Y. Chen, and R. Norte, Gravitational wave signatures of the absence of an event horizon. I. Nonradial oscillations of a thin-shell gravastar, *Phys. Rev. D* **80**, 124047 (2009).
- [25] V. Cardoso, L. C. B. Crispino, C. F. B. Macedo, H. Okawa, and P. Pani, Light rings as observational evidence for event horizons: Long-lived modes, ergoregions and nonlinear instabilities of ultracompact objects, *Phys. Rev. D* **90**, 044069 (2014).
- [26] J. Westerweck, Y. Sherf, C. D. Capano, and R. Brustein, Sub-atomic constraints on the Kerr geometry of GW150914, [arXiv:2108.08823](https://arxiv.org/abs/2108.08823).
- [27] J. Keir, Slowly decaying waves on spherically symmetric spacetimes and ultracompact neutron stars, *Classical Quantum Gravity* **33**, 135009 (2016).
- [28] V. Cardoso, L. C. B. Crispino, C. F. B. Macedo, H. Okawa, and P. Pani, Light rings as observational evidence for event horizons: Long-lived modes, ergoregions and nonlinear instabilities of ultracompact objects, *Phys. Rev. D* **90**, 044069 (2014).
- [29] P. V. P. Cunha, E. Berti, and C. A. R. Herdeiro, Light-Ring Stability for Ultracompact Objects, *Phys. Rev. Lett.* **119**, 251102 (2017).
- [30] P. Bizon and A. Rostworowski, On Weakly Turbulent Instability of Anti-de Sitter Space, *Phys. Rev. Lett.* **107**, 031102 (2011).
- [31] J. L. Friedman, Ergosphere instability, *Commun. Math. Phys.* **63**, 243 (1978).
- [32] G. Moschidis, A proof of Friedman's ergosphere instability for scalar waves, *Commun. Math. Phys.* **358**, 437 (2018).
- [33] J. Keir, Evanescent ergosurface instability, *Anal. Part. Diff. Eq.* **13**, 1833 (2020).
- [34] R. Brito, V. Cardoso, and P. Pani, Superradiance: New frontiers in black hole physics, *Lect. Notes Phys.* **906**, 1 (2015).
- [35] S. Chandrasekhar, The effect of gravitational radiation on the secular stability of the Maclaurin spheroid, *Astrophys. J.* **161**, 561 (1970).
- [36] J. L. Friedman and B. F. Schutz, Secular instability of rotating Newtonian stars, *Astrophys. J.* **222**, 281 (1978).